

---

Unterschrift des Betreuers



---

**Technische  
Universität  
Wien**

Vienna University of Technology

---

# DIPLOMARBEIT

---

## Injection of a Quantum Cascade Laser into a High-Finesse Optical Resonator

Using Pound-Drever-Hall Frequency Stabilization

---

Ausgeführt am Institut für Angewandte Physik (E134)  
und am Institut für Chemische Technologien und Analytik (E164)  
der Technischen Universität Wien

unter der Anleitung von Ao.Univ.Prof. Dipl.-Ing. Dr.techn. Martin Gröschl  
Ao.Univ.Prof. Dipl.-Ing. Dr.techn. Bernhard Lendl  
und Projektass. Dipl.-Ing. Mag.rer.nat Johannes Paul Waclawek

durch

**Volker Christian Bauer**

Breitenseer Straße 76/1/15,  
1140 Wien

---

Datum

---

Unterschrift (Student)

# Contents

<b>1</b>	<b>Introduction and Theoretical Basis</b>	<b>9</b>
1.1	Quantum Cascade Laser . . . . .	10
1.1.1	Natural Linewidth of Quantum Cascade Lasers . . . . .	12
1.2	Wave Optics, Gaussian Beams and Optical Resonators . . . . .	14
1.2.1	Wave Optics . . . . .	14
1.2.2	Gaussian Beams . . . . .	16
1.2.3	Optical Resonators . . . . .	20
1.2.4	Mode Matching of Gaussian Beams . . . . .	26
1.3	Pound-Drever-Hall (PDH) Laser Frequency Stabilization . . . . .	28
<b>2</b>	<b>Experimental Setup and Investigations</b>	<b>35</b>
2.1	Basic Experimental Setup . . . . .	36
2.2	Technical Equipment . . . . .	38
2.3	Laser Beam Alignment and Cavity Setup . . . . .	45
2.3.1	Cavity Parameters . . . . .	46
2.3.2	Mode-matching Calculation . . . . .	48
2.4	Influence of Cavity Parameters on the PDH Error Signal . . . . .	51
2.5	Electrical Noise . . . . .	53
2.5.1	Inherent Electronic Noise . . . . .	54
2.5.2	Grounding and Shielding for Noise-Improvement . . . . .	56
2.6	System Noise Investigations and Countermeasures . . . . .	60
2.7	Experimental Approaches . . . . .	68
<b>3</b>	<b>Results and Discussion</b>	<b>71</b>
3.1	Summary and Conclusion . . . . .	79
3.2	Outlook . . . . .	80
	<b>Bibliography</b>	<b>81</b>



## **Acknowledgements**

I want to thank *Bernhard Lendl* for making the offer to this work, and for giving me trust and great financial support. *Martin Gröschl*, for his assistance from the Institute of Applied Physics, his precious hints in noise-reduction techniques and grounding measures, and for providing a spectrum analyzer as a valuable instrument.

*Johannes Paul Waclawek*, for the ongoing and enjoyable talks, the prolific coffee-breaks, and the tremendous support in the lab and throughout the entire work.

*Christian Kristament*, from whom I learned some practical electronics before he left our institute, and finally, *Harald Moser*, for supporting me with useful hints and parts in the lab, and for being an all-time fountain of fun.

Last but not least I want to say thanks to *every-one* at the Institute of Chemical Technologies and Analytics for providing the pleasing conditions that I was experiencing during the course of this master thesis.

*“I have not failed.  
I’ve just found  
10,000 things that  
won’t work.”* [\[35\]](#)

Thomas A. Edison (1847-1931)  
Inventor of the light bulb

*Für meine Eltern, Hans und Gerda Bauer.*

# Abstract

In this work the experimental realization of frequency stabilizing a mid-infrared continuous wave distributed feedback quantum cascade laser by use of the Pound-Drever-Hall technique with a high-finesse optical resonator as a stable optical reference was investigated. As a consequence of this frequency stabilization the build-up of light intensity within the resonator should have been investigated for its practical purpose in spectroscopic applications. After some research of the respective literature and the selection of some specific components for the setup it was built up in the lab. Some adaptations were made compared to the suggestions of the literature in order to comply with the requirements of a mid-infrared quantum cascade laser. Due to the presence of electronic noise and ongoing failure of resonant conditions on a repeatable basis, the focus was set on noise investigation, which led to an improvement of the laser system's noise performance. Finally, it was possible to acquire weak signals that indicated the partial emergence of resonant conditions on a short time-scale. The coherence time of the laser was identified to be the most critical parameter for producing resonance when injecting laser light into an optical resonator. The results of this work pave the way for further practical approaches. With no doubt additional investigations have to be carried out but would exceed the extent and time-efforts of this master thesis.

## Glossary of used Mathematic Symbols

$A(\vec{r})$	.....	complex beam amplitude
$c$	.....	speed of light in vacuum
$F(\omega)$	.....	complex reflection coefficient of a resonator
$\mathcal{F}$	.....	finesse
$k$	.....	modulus of the wave-vector $k =  \vec{k}  = 2\pi/\lambda$
$L$	.....	resonator length
$\lambda$	.....	wavelength
$n$	.....	refractive index
$\nu$	.....	frequency
$g_1, g_2$	.....	g-parameters of a spherical mirror resonator
$q_i$	.....	complex q-parameter at position $i$
$\vec{r}$	.....	position vector in 3-dim space $(x, y, z)$
$r_n$	.....	radius of curvature of a mirror $n$
$R$	.....	reflection coefficient
$R(z)$	.....	radius of curvature of a Gaussian beam
$t$	.....	time
$T$	.....	transmission coefficient
$\tau_{\text{coh}}$	.....	coherence time
$U(\vec{r}, t)$	.....	time-dependent complex beam amplitude
$U(\vec{r})$	.....	time-independent complex beam amplitude
$W_0$	.....	beam waist radius of a Gaussian beam
$W(z)$	.....	beam radius of a Gaussian beam
$\omega$	.....	angular frequency $\omega = 2\pi\nu$ (e.g. of the carrier wave)
$\Omega$	.....	modulation angular frequency (of the sidebands)
$z_0$	.....	Rayleigh-range of a Gaussian beam



# Zusammenfassung

In der vorliegenden Arbeit wurde die experimentelle Realisierung der Frequenzstabilisierung eines Quantenkaskadenlasers durch die Pound-Drever-Hall Technik anhand eines optischen Resonators mit hoher Finesse als stabile optische Referenz untersucht. Als Konsequenz dieser Frequenzstabilisierung hätte der Anstieg der Lichtintensität im Inneren des Resonators auf seine praktische Anwendbarkeit in spektroskopischen Anwendungen untersucht werden sollen. Nach dem Studium der einschlägigen Literatur und der Auswahl passender Komponenten wurde der experimentelle Aufbau im Labor vorgenommen. Einige Anpassungen wurden dabei gemacht, um die Vorgaben der Literatur an die Erfordernisse eines Quantenkaskadenlasers anzupassen, welcher im mittleren Infrarot emittiert. Aufgrund des vorhandenen elektronischen Rauschens und der nicht erzeugbaren Resonanz innerhalb des Resonators auf reproduzierbarer Basis, wurde der Fokus auf die Untersuchung dieses Rauschens gelegt, was zu einer Verbesserung des System-Rauschens führte. Am Ende war es möglich, schwache Signale zu erfassen, welche auf einen teilweisen und kurzzeitigen Aufbau resonanter Bedingungen schließen lassen. Die Kohärenzzeit des Lasers wurde als kritischster Parameter identifiziert, um Resonanz innerhalb eines optischen Resonators zu erzeugen. Die Resultate dieser Arbeit ebnen den Weg für weitere praktische Ansätze. Ohne Zweifel müssen zusätzliche Nachforschungen angestellt werden, welche jedoch den Umfang und zeitlichen Rahmen dieser Diplomarbeit übersteigen würden.

# Chapter 1

## Introduction and Theoretical Basis

Quantum cascade lasers (QCL) operate from the mid-infrared (mid-IR) region to the far terahertz region of the electromagnetic spectrum, and are nowadays one of the most beneficial light sources in the field of infrared spectroscopy (e.g. [2, 3]). Optical resonators have a wide field of application in spectroscopy (e.g. [4]). Absorption spectroscopy is based on the quantized absorption of electromagnetic radiation by excitation of rotations and vibrations in molecules. If an absorbing medium is located between the mirrors of an optical resonator, the interaction length of the light field with the absorbing medium is increased due to the multiple reflections. As a consequence the detection sensitivity can be enhanced depending on the reflectivity of the used mirrors, especially if resonant conditions are present. Some of the existing techniques are not based on cavity resonance but in this work it shall be investigated which requirements have to be experimentally met to enhance the power build-up of a QCL in combination with an external optical resonator to produce resonance. If the light waves of a laser source are actively controlled to produce constructive interference within an external resonator, one would observe an intensity increase according to the mirror reflectivity therein. In order to achieve resonant conditions the laser frequency has to be stabilized because the linewidth of a free running laser source is typically larger than the linewidth of a high-finesse optical resonator, which would lead to poor coupling of laser power into the resonator. This frequency stabilization can be achieved by using an optical resonator as a stable reference for the laser source, and by applying electronic feedback from the reference to the source.

In the following sections an overview of the theory and concepts that are fundamental for this work is given. A brief introduction about QCLs and their operational

principle is followed by a short discussion about the natural linewidth of laser sources. Afterwards some of the basics of wave optics and Gaussian beams are presented, which is of fundamental importance for laser beam calculations. Subsequently, some theory on optical resonators is introduced, together with the basic equations that are needed further on. Using the insight of these chapters it might be obvious that stabilizing the laser frequency is critical for producing resonance within a high-finesse optical resonator. A detailed description of the Pound-Drever-Hall (PDH) frequency stabilization technique will be given in the final section of this introduction.

## 1.1 Quantum Cascade Laser

A quantum cascade laser (QCL) is a semiconductor laser device based on intersub-band transitions of electrons in a periodic quantum well heterostructure. The first experimental realization of a QCL was published in the year 1994:

“Electrons streaming down a potential staircase sequentially emit photons at the steps. The steps consist of coupled quantum wells in which population inversion between discrete conduction band excited states is achieved by control of tunneling.” [1]

In contrast to conventional semiconductor diode lasers that are based on interband transitions where electrons and holes recombine to emit photons, it is not the band-gap of the involved materials which determines the emission-wavelength of a QCL but rather the width of the quantum wells and barriers of the active region. These layers are grown with molecular beam epitaxy (MBE) or metal-organic chemical vapor deposition (MOCVD) [2], and offer a wide range of wavelengths in the mid-IR and terahertz region. QCLs are unipolar devices, which means that only electrons contribute to the lasing process. QCLs can either be operated in continuous wave or in pulsed mode. In figure 1.1 the basic (simplified) working principle is shown by an illustration of the potential well staircase.

Semiconductor layers of a certain thickness are cascaded to produce regions of varying electric potential: active and injector regions. An electron from the injector region is driven into the active region by an applied electric field (voltage) into the uppermost energy state  $E_3$ . The tilt of the potential staircase arises from the applied voltage drop. A laser photon of energy  $E_{23} = h\nu = E_3 - E_2$  (where  $h$  is Planck's

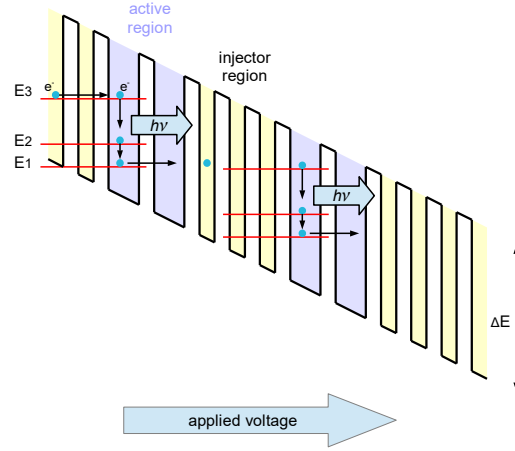


Figure 1.1: Operation principle of a quantum cascade laser

constant  $h = 6.626 \cdot 10^{-34}$  Js, and  $\nu$  the frequency in Hz of the electromagnetic wave) is emitted when electrons jump from the uppermost energy level  $E_3$  to a lower level  $E_2$ . The energy difference  $E_{23}$  is mainly determined by the thickness of the wells of the active region. As for any lasing process a population inversion is needed between energy levels  $E_3$  and  $E_2$ , hence the lifetime in level  $E_3$  has to be much larger than in  $E_2$ . In order to minimize the lifetime of electrons in state  $E_2$ , the energy level  $E_1$  is engineered to be about the energy of an optical phonon apart lower than  $E_2$ , which ensures rapid scattering from  $E_2$  to  $E_1$  (compare [2]).

After this process the electron from  $E_1$  stays in the conduction band, and is therefore available to emit another laser photon in the adjacent active region starting from  $E_3$  again. This cascading of active and injector regions, and the consequential recycling of electrons is responsible for the relatively large power output of QCLs in comparison to semiconductor diode lasers, since one electron can produce a photon in each of the transitions from  $E_3$  to  $E_2$  within the active region. In conventional diode lasers an electron recombines with a hole to produce a single photon and is consequently not capable of emitting another laser photon.

In principle a QCL structure emits a broad spectrum of wavelengths. However, QCLs can be designed to emit at a single wavelength and additionally feature some wavelength tunability, which makes them attractive in chemical sensor systems (see [3]). The wavelength tunability is based on the temperature dependency of the re-

fractive index of the QCL's waveguide material. Single mode operation with a small tuning range in a compact device is achieved by integrating a distributed feedback (DFB-QCL) grating structure into the active region [5]. An external and rotatable diffraction grating can be utilized to select specific wavelengths in an external cavity configuration (EC-QCL), which offers a wider tuning range than the DFB technology [6].

More than twenty years after their first experimental realization, QCLs are nowadays a superior light source in the mid-IR range (approximately from 3.0 - 24  $\mu\text{m}$  in wavelength) of the electromagnetic spectrum, covering fundamental vibrations in molecules including the so called molecular fingerprint region. It is possible to distinguish between different molecules based on their different characteristic rotational-vibrational spectrum. Applications reach from environmental monitoring such as trace gas sensing (e.g. quartz-enhanced photoacoustic spectroscopy or cavity ring-down spectroscopy) or liquid phase spectroscopy, frequency metrology and to a variety of other high-resolution spectroscopic applications [7].

### 1.1.1 Natural Linewidth of Quantum Cascade Lasers

The minimal linewidth  $\delta\nu$  of a laser device is limited as Schawlow and Townes investigated in 1958 [8] even before the first demonstration of a laser; they found that the minimal linewidth is limited by spontaneous emission and can be described by

$$\delta\nu = \frac{4\pi h\nu}{P}(\Delta\nu)^2. \quad (1.1)$$

Herein  $\Delta\nu$  is the half-width at half maximum (HWHM) intensity of a laser mode and  $P$  the power in the oscillating field; spontaneous emission adds waves of random phase ("zero-point fluctuations" [8]) to the stimulated coherent electromagnetic field, leading to a broadening of the linewidth. This restriction can be eventually interpreted in terms of a quantum limit and as a consequence of Heisenberg's uncertainty relation.

As a correction for the fundamental Schawlow-Townes limit (1.1) Henry gave 1982 an explanation for the linewidth broadening in single-mode semiconductor lasers by introducing a linewidth enhancement factor; he identified a change of the refractive index of the semiconductor with carrier density fluctuations, which couples phase and intensity fluctuations [9].

In contrast to conventional semiconductor lasers the refractive index of QCLs was expected to show only negligibly small variations at the peak of the gain curve in the initial work of 1994 [1]; therefore, the linewidth enhancement factor of QCLs would be close to zero, and one might assume the intrinsic linewidth similar to the Schawlow-Townes limit.

However, a theoretical investigation by Yamanishi et al. [10] in 2008 discovered the participation of ultrafast non-radiative relaxation processes from the uppermost energy level into the lower levels (for a QCL with a three level energy-scheme as presented above) that do not contribute to spontaneous emission, leading to a novel version of the Schawlow-Townes limit and to a narrower linewidth. Moreover, this theory contains the line-broadening by thermal photons that had been so far overlooked.

Bartalini et al. [11] experimentally verified these theoretic predictions in 2010; the experimental data showed the awaited behavior. Furthermore, the noise power spectral density (PSD) was lower than theoretically expected. This ultimately proofed that the QC laser type overcomes the Schawlow-Townes limit leading to narrower linewidth features.

They also investigated the noise in the absence of these ultrafast non-radiative relaxation processes, which lead to comparable noise features that can be observed in conventional semiconductor lasers [11] showing good coincidence with Henry's theory [9].

A common method to determine the frequency noise of a QCL is to convert the frequency fluctuations into intensity fluctuations, by the use of a side of a Doppler-broadened molecular line [7] of a gas molecule placed in the optical path of a QCL source, and by measuring the corresponding absorption of the laser signal with a photo-detector. The quantum-limited linewidth for a mid-IR QCL at room-temperature has been determined to be approximately 200 Hz<sup>1</sup> [7]. These results motivate that a large contribution to frequency noise may originate from the current source that drives a QCL. Low-noise current drivers are therefore an essential part when detecting the intrinsic noise of a QCL (see [13]).

Tombez et al. used a custom-made current driver with a current noise density lower than 350 pA/ $\sqrt{\text{Hz}}$  [12], which they found of having no broadening influence on the

---

<sup>1</sup>For comparison: this would mean a wavelength interval of  $1.4 \times 10^{-8}$  nm for the QCL employed in this work (which had a center wavelength of 4.59  $\mu\text{m}$ )

intrinsic linewidth of a 4.6  $\mu\text{m}$  DFB-QCL at room temperature. Moreover, they predicted this particular current driver to be sufficiently low-noise to improve the frequency stability of the DFB-QCL by implementing a feedback loop with a bandwidth in the order of 100 kHz.

## 1.2 Wave Optics, Gaussian Beams and Optical Resonators

The concept of wave optics extends conventional ray (geometric) optics by taking into account the wave nature of light. Based on wave optics the Gaussian beam is described, accounting for the fact that many laser types emit with a similar beam-profile. This applies for the QCL-source employed in this work as well. A Gaussian beam differs from a plane wave as it has curved wavefronts, and its lateral extension is of finite diameter; both, the radius of the wavefronts, and the diameter of the beam, change with the distance to the center of the beam. The latter leads to a diverging beam. Optical resonators are then described to familiarize with the involved formulas and for the comprehension of terms like mode linewidth, finesse, and intensity build-up. The interference phenomena that arise during the operation of an optical cavity cannot be described by simple ray optics; here it is inevitable to use the description of the wave nature of light. The final subsection describes mode-matching, which is an essential technique to optimize the transferred power from a laser source into an optical resonator.

### 1.2.1 Wave Optics

A light wave can be described by a scalar wavefunction  $u(\vec{r}, t)$  with  $\vec{r} = (x, y, z)$ , and is a solution of the wave equation<sup>2</sup> (1.2) traveling at the speed of light<sup>3</sup>  $c = \frac{c_0}{n}$  in a medium. In case of a homogeneous medium,  $n \geq 1$  is a real number, and is called index of refraction.

$$\Delta u(\vec{r}, t) - \frac{1}{c^2} \frac{\partial^2 u(\vec{r}, t)}{\partial t^2} = 0 \quad (1.2)$$

The wave equation (1.2) is a linear partial differential equation. Therefore, two solutions can be linearly superimposed giving another possible solution. This principle is fundamental, e.g. for the formation of standing waves, since they are a superposition

---

<sup>2</sup>Laplace operator  $\Delta = \nabla^2 = \frac{\partial^2}{\partial x^2} + \frac{\partial^2}{\partial y^2} + \frac{\partial^2}{\partial z^2}$

<sup>3</sup>Speed of light in vacuum:  $c_0 = 299792458 \text{ m/s}$

of incident and a reflected waves (see section 1.2.3). The wave-function  $u(\vec{r}, t)$  is given either by the electric  $E(\vec{r}, t)$  or the magnetic field  $B(\vec{r}, t)$ . This is of course a simplified description because one would have to treat these quantities as vectors, which is not possible in wave optics because it is a scalar theory. This would be part of a full electromagnetic theory of light, which offers the ability to describe e.g. polarization as well. Nevertheless, each component of the electric or magnetic field vector on its own has to be a solution of the wave equation (1.2) (compare [14], p.157). The following discussion stays in the simple picture of wave optics, since it will be sufficient for the description of a Gaussian beam and resonator optics.

Starting with a simple monochromatic wave one can write

$$u(\vec{r}, t) = a(\vec{r}) \cos(2\pi\nu t + \varphi(\vec{r})), \quad (1.3)$$

with the real amplitude  $a(\vec{r})$ , the frequency of the wave  $\nu = c/\lambda$ , with the wavelength  $\lambda$ , and the phase  $\varphi(\vec{r})$ . Equation (1.3) can also be written in a complex form, which will be important in section 1.3 Pound-Drever-Hall (PDH) Laser Frequency Stabilization for describing a phase-modulated beam:

$$U(\vec{r}, t) = U(\vec{r}) e^{i\omega t} = a(\vec{r}) e^{i\varphi(\vec{r})} e^{i\omega t}, \quad (1.4)$$

with the complex amplitude  $U(\vec{r})$  and the angular frequency  $\omega = 2\pi\nu$ . The relation between the real  $u(\vec{r}, t)$  (1.3) and the complex form of  $U(\vec{r}, t)$  (1.4) is given by  $u(\vec{r}, t) = \text{Re}(U(\vec{r}, t)) = \frac{1}{2}(U(\vec{r}, t) + U^*(\vec{r}, t))$ , where  $*$  denotes complex conjugation.

The intensity  $I$  of a monochromatic wave is given by

$$I(\vec{r}) = |U(\vec{r}, t)|^2, \quad (1.5)$$

and is therefore a time-invariant quantity.

In the case of a plane wave with  $|\vec{k}| = 2\pi/\lambda$  the complex amplitude is (compare [14], p. 44)

$$U(\vec{r}) = A e^{-i\vec{k} \cdot \vec{r}}, \quad (1.6)$$

whereas  $A$  is a complex constant and denoted as the complex envelope. A paraxial wave that propagates along the z-axis has a varying complex envelope  $A(\vec{r})$ . There-



fore, one writes (compare [14], p. 47):

$$U(\vec{r}) = A(\vec{r})e^{-ikz}. \quad (1.7)$$

It can be shown (compare [14], p. 48), that if the beam envelope varies slowly within the distance of a wavelength  $\lambda$ , and the complex envelope  $A(\vec{r})$  satisfies certain conditions (see [14], p. 48, eqn. 2.2-21. 2.2-22), the paraxial wave is a solution of the paraxial Helmholtz equation (1.8):

$$\left( \frac{\partial^2}{\partial x^2} + \frac{\partial^2}{\partial y^2} \right) A - i2k \frac{\partial A}{\partial z} = 0. \quad (1.8)$$

One of the possible solutions of this differential equation is the Gaussian beam (1.9) ([14], p. 76), which will be the object of the following section. To summarize this: one possible solution of the Helmholtz equation is the paraxial wave. By using some assumptions regarding these paraxial waves one obtains another differential equation, i.e. the paraxial Helmholtz equation.

## 1.2.2 Gaussian Beams

The complex envelope of a Gaussian beam is a solution of the paraxial Helmholtz equation (1.8) (see [14], p. 76). It is given by

$$A(\vec{r}) = \frac{C_1}{q(z)} e^{-ik \frac{x^2+y^2}{2q(z)}}. \quad (1.9)$$

$C_1$  is a constant;  $q(z) = z + iz_0$  is denoted as the complex beam-parameter;  $z_0$  is the Rayleigh-range. The complex q-parameter of a Gaussian beam is given by

$$\frac{1}{q(z)} = \frac{1}{R(z)} - i \frac{\lambda}{\pi W^2(z)}, \quad (1.10)$$

which fully characterizes a Gaussian beam.  $R(z)$  is the radius of curvature of a wavefront;  $W(z)$  is the beam radius at position  $z$ . Since the wavefronts are planar at the beam waist, the radius of curvature is infinite, and the q-parameter becomes purely imaginary.

The complex beam amplitude  $U(\vec{r})$  is (compare [14], p. 77)

$$U(\vec{r}) = C_0 \frac{W_0}{W(z)} e^{-\frac{x^2+y^2}{W^2(z)}} e^{-i(kz - k \frac{x^2+y^2}{2R(z)} + \tan^{-1} \frac{z}{z_0})}, \quad (1.11)$$

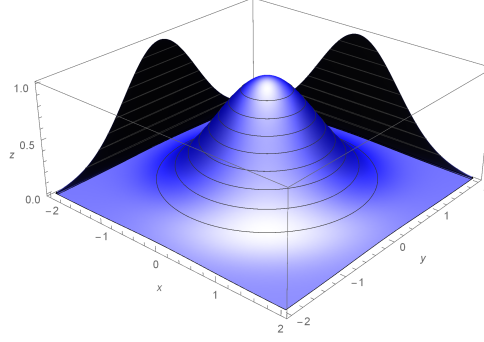


Figure 1.2: Shape of the Gaussian beams intensity  $I(\rho, 0)$  for a wave propagating in z-direction, in the plane  $z = 0$  :  $I(\rho, 0) \sim e^{-(x^2+y^2)}$ . Plotted in arbitrary units. Additionally, the projection onto the x- and y-plane is shown.

with a new constant  $C_0 = \frac{C_1}{I_{z0}}$ . It is given here for the purpose of completeness. The meaning of the newly introduced quantities will be clear in the subsequent. The phase of a Gaussian beam differs from that of a plane wave, which would be  $kz$ . According to (1.11), the phase of a Gaussian beam is given by  $kz + k \frac{x^2+y^2}{2R(z)} - \tan^{-1} \frac{z}{z_0}$ . Herein,  $\zeta(z) = \tan^{-1} \frac{z}{z_0}$  is known as the Gouy-phase (see [14], p. 81).

Referring to (1.5), the intensity of a Gaussian beam is obtained by taking the absolute square of the complex amplitude  $U(\vec{r})$ , i.e.  $I(\vec{r}) = |U(r)|^2$ , which leads to (compare [14], p. 79)

$$I(\rho, z) = \frac{2P}{\pi W^2(z)} e^{-\frac{2\rho^2}{W^2(z)}}. \quad (1.12)$$

It is plotted for  $z = 0$  in figure 1.2. We have used polar coordinates due to the radial symmetry, and introduced  $\rho = \sqrt{x^2 + y^2}$  and the power in the beam

$$P = \frac{1}{2} I_0 W_0^2 \pi, \quad (1.13)$$

with  $I_0 = |C_0|^2$ . Equation (1.13) is obtained by integrating the intensity over any of the transverse planes at a position  $z = \text{const}$  (compare [14], p. 78). As one can see, the spatial intensity profile, in a perpendicular plane with respect to the direction of propagation, is of a Gaussian shape, which explains the origin of its denomination. From equation (1.12) one concludes, that the beam intensity not only varies in radial direction with  $\rho$  but also in z-direction along the axis.

Consequently, the properties of a Gaussian beam can be summarized as follows (compare with figure 1.3): the beam power is concentrated along the beam axis. The

distribution of its intensity in any transverse plane is given by a symmetric Gaussian function, centered at the beam axis, where the intensity is a maximum. At the beam waist the diameter of the beam is a minimum and becomes larger with increasing distance from the waist, which means a diverging beam shape from the center into both directions along the optical axis. This leads to a lowering of the beam center intensity along the axis. The wavefronts of a Gaussian beam are planar at the beam waist and become spherical in the far field, hence, they are gradually curved in the near field, and almost planar in the far field.

For a Gaussian beam (see figure 1.3) with its waist located at  $z = 0$ , the beam width, i.e. the radius, is given by

$$W(z) = W_0 \sqrt{1 + \frac{z^2}{z_0^2}}, \quad (1.14)$$

with the radius  $W_0$  at the beam waist ( $z = 0$ )

$$W_0 = \sqrt{\frac{\lambda z_0}{\pi}}. \quad (1.15)$$

Equation (1.15) describes the laser beams minimal beam waist diameter  $2W_0$ , which is sometimes denoted as the spot-size. By rearrangement of equation (1.15), one

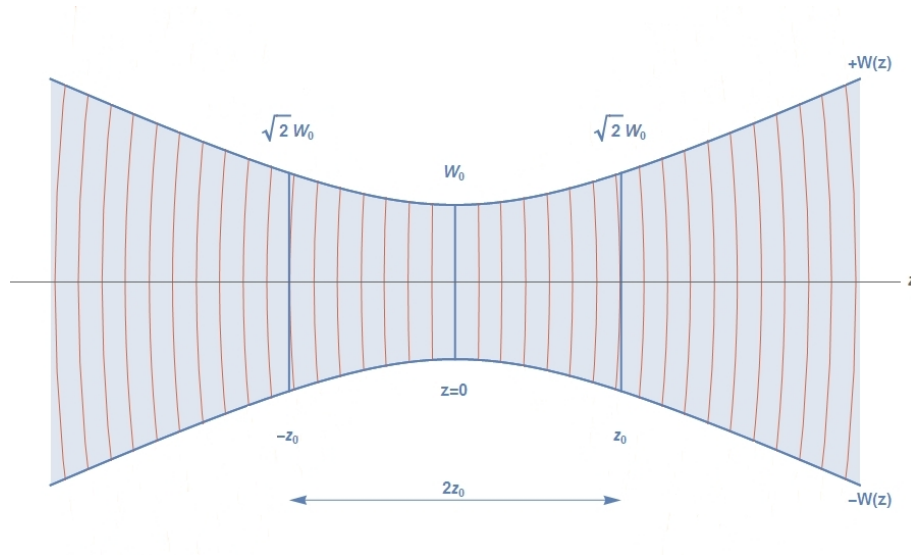


Figure 1.3: Gaussian beam with its envelope  $\pm W(z)$  and calculated curved wavefronts  $R(z)$ . The beam waist radius  $W_0$  is located at  $z = 0$ , the Rayleigh range  $2z_0$  is denoted and the corresponding waist radii are shown.

obtains  $z_0$ , the Rayleigh range of a Gaussian beam (1.16)

$$z_0 = \frac{\pi W_0^2}{\lambda}. \quad (1.16)$$

Hence, for a given wavelength, a Gaussian beam is completely characterized by defining either the waist size  $W_0$  or the Rayleigh range  $z_0$ . The radius of curvature (RoC) of the wavefronts is

$$R(z) = z + \frac{z_0^2}{z}, \quad (1.17)$$

which is infinite at the waist ( $z = 0$ ) and in the far field ( $z \rightarrow \infty$ ) with planar wavefronts. The minimum of the radius of curvature is located at a distance  $z_0$ , i.e. the Rayleigh range with  $R(z_0) = 2z_0$ .

The divergence angle  $\theta_0$  of a Gaussian beam is described by

$$\theta_0 = \frac{\lambda}{\pi W_0}. \quad (1.18)$$

This equation is of fundamental importance and states that for a certain wavelength the angle of divergence of a Gaussian beam is defined by the spot-size and vice versa. Lowering the spot-size will therefore result in a higher beam divergence, while increasing the spot-size would lower the beam divergence. This circumstance is utilized if it is the aim to focus a laser beam to the smallest spot-size possible. In a first step the beam is widened up by a lens to get a low beam divergence (beam expander); the resulting rays are almost parallel and can then be focused into the focal point of a second lens to produce the smallest spot-size possible, limited by wave-diffraction only.

To calculate the beam-propagation of a Gaussian beam through optical components or surfaces the ABCD-law (2.1), in terms of paraxial approximation, can be applied

$$q_2 = \frac{Aq_1 + B}{Cq_1 + D}. \quad (1.19)$$

In this equation the incident beam is characterized by the complex beam-parameter  $q_1$ , and is transformed by the matrix-elements of a certain ABCD-matrix (ray-transfer matrix) into the beam-parameter  $q_2$ . In the following it is assumed that a light ray travels from left to right, i.e. in the positive x-direction. Furthermore, one should always stay within the general convention, that all radii of optical boundary-surfaces

are counted as negative if the center of the corresponding circle lies to the left and vice versa ([16], p. 271). The ABCD-Matrix<sup>4</sup> of e.g. a thin lens with focal length  $f$  is

$$\begin{pmatrix} 1 & 0 \\ -1/f & 1 \end{pmatrix}.$$

The ABCD-matrix of space propagation in a medium with an index of refraction  $n$  over the distance  $d$  is given by

$$\begin{pmatrix} 1 & d/n \\ 0 & 1 \end{pmatrix}.$$

The refraction of a paraxial ray passing through a spherical surface with radius  $R$ , separating two materials with refractive indices  $n_1$  and  $n_2$ , is described by (compare [16], p. 288)

$$\begin{pmatrix} 1 & 0 \\ \frac{n_1 - n_2}{R} & 1 \end{pmatrix}$$

If optical components are cascaded in a beam-path (e.g. lenses, mirrors, boundary surfaces between different media etc.) the resulting ABCD-matrix is

$$M_{ABCD} = M_N M_{N-1} \dots M_2 M_1, \quad (1.20)$$

wherein  $M_1$  represents the ray-transfer matrix of the first optical component in the beam-path, and  $M_N$  the last one, respectively. These equations will be used in section 2.3.2 to calculate the parameters for a mode-matching lens in order to optimize the power transfer from the laser beam into the optical resonator.

### 1.2.3 Optical Resonators

An optical resonator can store light of a certain frequency and for a certain time, depending on its physical properties. There exist several types of optical resonators; the basic configuration consists of two plane-parallel mirrors called Fabry-Pérot etalon (or planar-mirror resonator). One major disadvantage of it arises, when the angle of incidence is slightly inclined or the mirrors are not perfectly parallel aligned; the rays are then likely to escape from the resonator. Another configuration that uses spherically curved mirrors is called spherical mirror resonator. Here the multiple beam

---

<sup>4</sup>Reflection from a spherical mirror with radius  $R$ :  $\begin{pmatrix} 1 & 0 \\ 2/R & 1 \end{pmatrix}$ ,  $R < 0$ : concave,  $R > 0$ : convex

reflections are easier held in place by the focusing effect of the curved mirrors, which makes a cavity of this type less critical to mis-alignment. There are even more types of resonators, e.g. a combination of one flat and one curved mirror or more than two mirrors forming a ring resonator. In the following the Fabry-Pérot etalon is used as a starting point, and then the equations for the spherical mirror resonator are described, since the latter was employed in this work.

If one considers a light wave propagating in  $z$ -direction with an electrical field amplitude  $U_0$

$$U(\vec{r}, t) = U_0 e^{ik(z-ct)}, \quad (1.21)$$

and perpendicular incidence on the first (or entrance) mirror of a Fabry-Pérot resonator (figure 1.4), one part of the beam intensity gets reflected, and another part gets transmitted. The amount of light that enters the cavity travels further on to the second mirror, and experiences another reflection and transmission. The light wave, that is reflected back from the second mirror, gets then reflected and transmitted again at the first mirror, and so forth. This multiple bouncing of interfering light waves is responsible for the amplification of optical power within the cavity but only when the resonance condition is met, which is, when the light waves interfere constructively within the cavity; that is only possible if the cavity's length  $L$  is an integer number  $q$  times the half wavelength  $\lambda$  of the incident light wave, i.e.

$$L = q \frac{\lambda}{2}. \quad (1.22)$$

If the mirrors are not perfectly reflecting, which is the case for any real mirror, this resonance-condition is loosened up with decreasing mirror-reflectivity. In this case, there will be some wavelength-interval where the cavity will be resonant on. That leads to the term finesse of an optical resonator (see equation 1.31).

To derive the resonance-condition presented above one has to solve the Helmholtz equation (1.23) [see [14], p. 368].

$$[\nabla^2 + k^2]U(\vec{r}) = 0 \quad \text{with} \quad k = \frac{2\pi\nu}{c} = \frac{\omega}{c} \quad (1.23)$$

Herein  $U(\vec{r})$  is the transverse component of the field amplitude of the electric field.

The Helmholtz equation (1.23) can be obtained from the wave equation (1.2) by

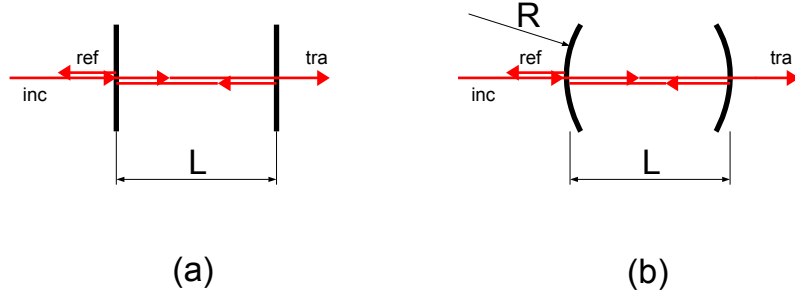


Figure 1.4: (a) Planar mirror resonator, (b) spherical mirror resonator

separating a generic wavefunction  $u(\vec{r}, t)$  into a product of the form

$$u(\vec{r}, t) = U(\vec{r})T(t) \quad (1.24)$$

in order to reduce the complexity of this partial differential equation, and to end up with a *time-independent* equation for the electric field-amplitude. Putting (1.24) into the wave-equation (1.2) one obtains

$$\frac{\nabla^2 U(\vec{r})}{U(\vec{r})} = \frac{1}{c^2 T(t)} \frac{\partial^2 T(t)}{\partial t^2} \quad (1.25)$$

Since the left hand-side of equation (1.25) only depends on the position  $\vec{r}$ , and the right hand-side only depends on the time  $t$ , it must be equal to a constant number that can be set  $-k^2$  without loss of generality, therefore ending up with equation (1.23).

Introducing boundary-conditions for the electric field amplitude  $U(\vec{r})$  at the lossless mirror surfaces, assuming that the first mirror is located at  $z = 0$ , and the second mirror at  $z = L$ , respectively

$$U(\vec{r}) = 0 \quad \text{at} \quad z = 0 \quad \text{and} \quad z = L \quad (1.26)$$

so that the Helmholtz-equation can be solved for  $kL = n\pi$ ; that represents a standing wave (1.27)

$$U(\vec{r}) = A \sin(kz) \quad (1.27)$$

with a constant amplitude  $A$ . The boundary-conditions (1.26) require  $q$  to be a whole number

$$k_q = q \frac{\pi}{L} \quad \text{for } q = 1, 2, \dots \quad (1.28)$$

so that on resonance the corresponding frequencies are restricted to

$$\nu_q = q \frac{c}{2L} \quad \text{for } q = 1, 2, \dots \quad (1.29)$$

wherein  $q$  is denominated as the mode number. The distance of two adjacent resonances in frequency space  $\nu_{\text{FSR}}$  is called the free spectral range (FSR) of an optical resonator

$$\nu_{\text{FSR}} = \frac{c}{2L}. \quad (1.30)$$

This expression shows that the mode-spacing decreases with increasing cavity length, i.e. an increase of the mode-density. The formulas which describe optical resonators following below, tightly follow reference [14] (Chapter 10, Resonator Optics). The

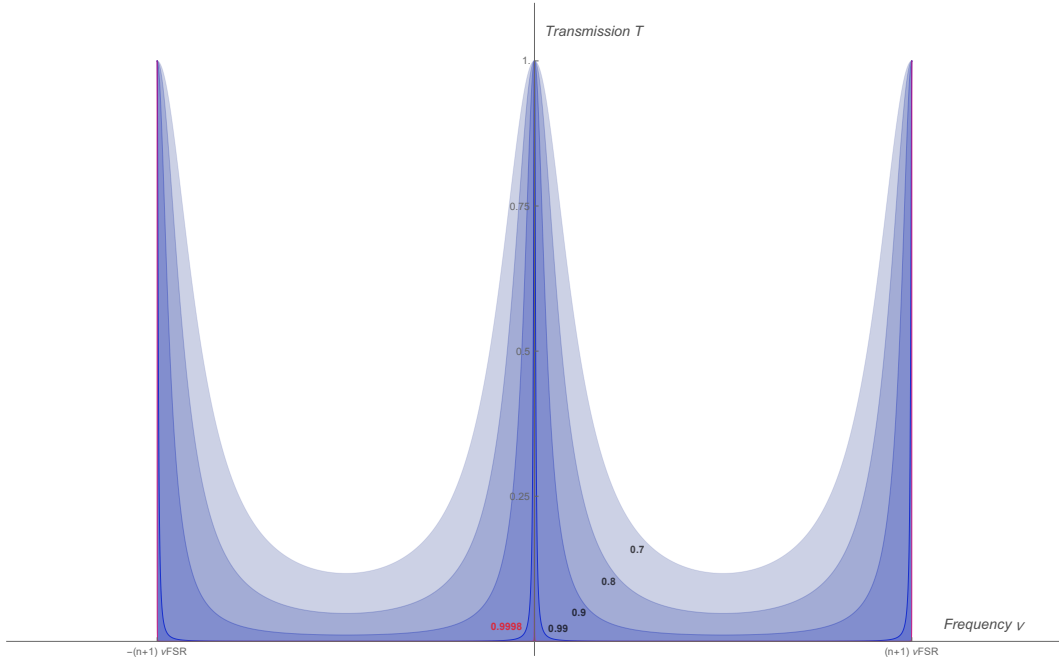


Figure 1.5: Transmission of an optical resonator for different values of mirror reflectivity:  $R = 0.7, 0.8, 0.9, 0.99$  and  $0.9998$ ; the narrowing of the linewidth with increasing reflectivity is illustrated

finesse  $\mathcal{F}$  of an optical cavity is given by

$$\mathcal{F} = \frac{\pi\sqrt{R}}{1-R} \quad (1.31)$$



with the mirror reflectivity  $R$ . As mentioned above, the sharp lines of resonances that are separated by the FSR get widened up if losses are introduced by the mirrors; the linewidth broadening arises from a phase shift of two successive reflections of a wave, generated in every single round-trip (see [14], p. 371), and then consequently, by superposition of these phase-shifted waves; the amplitude is attenuated in each reflection, since the reflection coefficient is  $R < 1.0$ ; the resulting characteristic is plotted<sup>5</sup> in figure 1.5, and is given by the Airy-function (e.g. see [16], p. 312); the full-width at half maximum (FWHM) of one resonance-peak is given by

$$\Delta\nu \approx \frac{\nu_{\text{FSR}}}{\mathcal{F}}. \quad (1.32)$$

Basically there are two sources of losses: imperfect reflection at the mirrors (including fraction losses), and losses  $\alpha_s$  due to absorption and scattering within the cavity medium, which can in sum be described by an effective overall loss coefficient  $\alpha_r$  (compare [14], p. 374):

$$\alpha_r = \alpha_s + \frac{1}{2L} \ln \frac{1}{R^2} \approx \alpha_s + \frac{1-R}{L}. \quad (1.33)$$

The approximation-sign in equation (1.33) refers to identical mirror reflectivities and high-reflectivity mirrors ( $R_1 = R_2 = R \approx 1$ ). The finesse  $\mathcal{F}$  can now also be written in terms of the loss coefficient  $\alpha_r$ :

$$\mathcal{F} \approx \frac{\pi}{\alpha_r L}. \quad (1.34)$$

In a real system, losses will always lower the finesse of a resonator due to possible presence of absorbing media or reflection losses introduced by imperfect or unclean mirror surfaces. One way to examine the real finesse of a system would be to determine the ratio of  $\nu_{\text{FSR}}/\Delta\nu$  from equation (1.32) by actual measurement.

The lifetime  $\tau_p$  of a photon can be interpreted in terms of a time-frequency uncertainty relation as

$$\tau_p = \frac{1}{c\alpha_r} = \frac{1}{2\pi \Delta\nu}, \quad (1.35)$$

---

<sup>5</sup>In this vector-graphic one may zoom in and take a view on the narrowest linewidth for  $R = 0.9998$ , which applies to the high-reflectivity mirrors employed in this work

leading to the linewidth broadening mentioned above.  $\tau_p$  is also called cavity ring-down time ([17], p. 2)<sup>6</sup>. If a light wave incident on a resonating optical resonator is blocked, the light intensity drops to  $1/e$  after the time  $\tau_p$ . Conversely, if a light wave with a frequency that matches the resonance frequency of the resonator is unblocked, the intensity builds up to  $(1 - 1/e)$  after the time  $\tau_p$ . The ring-down time can also be interpreted in terms of a response-time of a cavity, averaging over any intensity fluctuations of the incident beam, occurring within that time-span.

The intensity build-up within a resonant optical cavity, as a consequence of multiple reflections and ongoing constructive interference, leads to an intra-cavity intensity of (compare [18], eqn. 4.78)

$$I_{\text{int}} = \frac{1}{(1 - R)} \frac{I_0}{1 + (2\mathcal{F}/\pi)^2 \sin^2(\pi\nu/\nu_{FSR})}. \quad (1.36)$$

with the intensity of the incident wave  $I_0 = |U_0|^2$ . This intra-cavity intensity is  $1/T = 1/(1 - R)$  times larger than the intensity that is transmitted out of the resonator. The build-up factor  $g_{\text{build-up}}$  that is generated within an optical resonator<sup>7</sup> with no losses is therefore given by

$$g_{\text{build-up}} = \frac{1}{1 - R}. \quad (1.37)$$

Considering the law of energy conservation, the transmitted intensity of an optical resonator with no losses, nor any internal gain, in a steady state has to be equal to the input intensity; otherwise the intra-cavity field would diverge in an unphysical way.

**Spherical Mirror Resonator** Up to now considerations have been in the picture of the planar mirror resonator. The spherical mirror resonator introduces more complexity and thereby some interesting phenomena such as Gaussian modes and higher order modes. The characterizing property of a spherical mirror resonator is based on the curvature of the mirrors. Not every combination of mirror radii of curvature  $r_i$  and resonator lengths  $L$  leads to a usable and efficient resonator. The confinement condition for a stable spherical mirror resonator can be derived by use of the

<sup>6</sup>The numeric value of the cavity ring-down or decay time is basically the same as the ring-up or build-up time - but one has to distinguish the different context

<sup>7</sup>According to a mirror reflectivity of 0.9998, this intensity build-up would be given by a factor of 5000.

ray-transfer matrix formalism (compare [14], p. 379) to

$$0 \leq \left(1 + \frac{L}{r_1}\right) \left(1 + \frac{L}{r_2}\right) \leq 1, \quad (1.38)$$

with the g-parameters  $g_1$  and  $g_2$ , which are given by<sup>8</sup>

$$g_n = \left(1 + \frac{L}{r_n}\right) \quad n = 1, 2. \quad (1.39)$$

All combinations that do not comply with condition (1.38) would lead to an unstable resonator with increased losses. The waist-size (radius) that builds up within a spherical resonator can now be expressed with these g-parameters (see [17], p. 31):

$$W_0 = \sqrt{\frac{L\lambda}{\pi}} \left[ \frac{g_1 g_2 (1 - g_1 g_2)}{(g_1 + g_2 - 2g_1 g_2)^2} \right]^{1/4}, \quad (1.40)$$

which is an important quantity for mode-matching (see section 1.2.4).

So far only the fundamental modes were considered, i.e. the Gaussian  $\text{TEM}_{mn} \rightarrow \text{TEM}_{00}$  modes<sup>9</sup>. The paraxial Helmholtz equation also provides solutions, known as the Hermite-Gaussian beams (see [14], p. 94), based on Hermite-Gaussian polynomials that are characterized by the mode numbers  $(m, n)$  and lead to certain patterns of the beam intensity. Nevertheless, these modes can be part of a stable resonator configuration, since the wavefronts are of the same paraboloidal form as for the Gaussian beam. However, the resonance frequencies of these modes differ from the one provided by the Gaussian mode (see [14], p. 387). In order to maximize the power build-up within an optical resonator at a certain resonance frequency, it is therefore appreciable to select only modes with a single resonance frequency. This is done by mode-matching, which leads to the Gaussian  $\text{TEM}_{00}$  modes.

## 1.2.4 Mode Matching of Gaussian Beams

Improper alignment or a mismatch of the beam waist size of a Gaussian beam, that is incident on a stable spherical mirror resonator configuration, leads to off-axis spatial eigenmodes, and therefore not only to fundamental Gaussian modes within the resonator ( $\text{TEM}_{00}$ ) but also to higher order modes ( $\text{TEM}_{mn}$ ,  $m, n > 1$ ) [22]. The

<sup>8</sup>The radius  $r_n$  has to be taken negative for a concave mirror

<sup>9</sup>TEM (transverse electro magnetic). The mode numbers  $m, n$  (corresponding to the transverse beam directions  $x, y$ ) indicate the respective order of the underlying Hermite-polynomials

first is up to practical beam alignment technique, which is described in section 2.3, while the latter has to be dealt with in advance by some calculation, and will be the object in the following.

In order to optimize the power that can be coupled from a laser beam into an optical resonator, and to excite only the fundamental  $\text{TEM}_{00}$  Gaussian modes, it is indispensable to match the laser beam waist to the one that evolves within the resonator. To show this in practice a detailed mode-matching calculation will be carried out in chapter 2.3.2, while the theoretical background is addressed here.

Consider an optical resonator consisting of two spherical mirrors and a laser-source emitting a beam with a Gaussian profile. As presented in section 1.2.2, a Gaussian beam is fully characterized by its wavelength and waist-size. Another certain property of a Gaussian beam is the radius of curvature of the wavefronts given by equation (1.41) or equivalently by (1.17). Here the coordinate in propagation direction  $z$  is measured with respect to the position of the waist, where  $z = 0$ .

$$R(z) = z \left( 1 + \left( \frac{\pi W_0^2}{\lambda z} \right)^2 \right) \quad (1.41)$$

It might be intuitively clear that if the diameter of an incident laser beam is much larger than a resonator mirror's diameter, losses will be introduced; but another critical parameter is the radius of curvature of the wave-fronts of a Gaussian beam, in comparison to the radius of a curved cavity mirror. Hence, the aim of a mode-matching calculation is to match the beam waist size that evolves within an optical resonator to that of the laser beam at the cavity's waist position. As one has seen above, the waist that evolves within a cavity depends on the radius of the curved mirrors and the cavity length (see equation 1.40). Equivalently speaking, one could say that the aim of a mode-matching calculation is to fit the radius of curvature of the beam to that of the curved cavity mirror at the boundary surface. That both of these objectives are one and the same follows from the fact that a Gaussian beam is fully characterized by its waist-size (for a given wavelength).

One possible mathematical approach to manage this calculation is using the Gaussian q-parameter formalism in combination with the ray-transfer matrix formalism (see equation 2.1). First, the beam waist diameter  $W_1$  of the incident laser beam and its position  $z_{W1}$  has to be determined (see figure 1.6). This leads to the complex

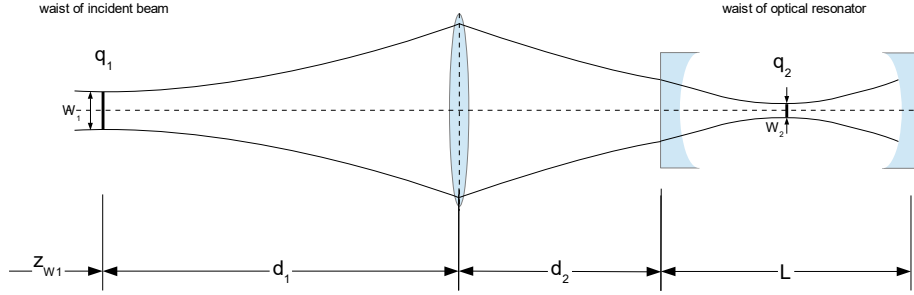


Figure 1.6: Mode-matching a laser beam to an optical resonator

$q$ -parameter  $q_1$ , which is purely imaginary at the beam waist (where  $\text{RoC} \rightarrow \infty$ ). In most cases the beam waist size and position will be measured experimentally, since this is the most accurate method. Alternatively one could calculate these parameters, but this would be effortful and time-consuming. Moreover, the results could be inaccurate because of the underlying tolerances of used components (lenses, pinholes, etc.) and due to an uncertainty in lens positioning. The beam waist within the cavity can now be calculated with equation (1.40), leading to the complex  $q$ -parameter  $q_2$ , which is again purely imaginary at the cavity's beam waist ( $\text{RoC} \rightarrow \infty$ ). Putting  $q_1$  and  $q_2$  into (2.1) and using a certain ABCD-Matrix that describes the entire beam propagation as follows: starting from a beam waist, passing the mode-matching lens, passing the entrance cavity-mirror and finally arrives at the waist of the cavity. This gives an equation that has to be solved for the unknown distances  $d_1$  and  $d_2$ , which describe the distance from the waist  $W_1$  of the incident beam to the mode-matching lens, and from this position to the entrance mirror of the cavity.

### 1.3 Pound-Drever-Hall (PDH) Laser Frequency Stabilization

The frequency stability of a tunable laser can be improved by use of the PDH-technique [20]. The basic idea of this method is to detect the reflected signal from a Fabry-Pérot cavity, and to control the laser frequency by an electronic feedback loop to hold the power that is reflected from the cavity at zero. This is possible be-

cause the optical back-reflection of a Fabry-Pérot resonator vanishes on resonance. The cavity resonance acts as a frequency-reference for the laser source. The PDH-technique is not only restricted to optical applications; it can be also realized with purely electrical components by use of RF-equipment [21]. E.D. Black has given an excellent introduction to this technique [19], which will be followed tightly in this section.

In the PDH-technique (see figure 1.7) the laser frequency (or equivalently the phase) is modulated with a local oscillator and a Pockels cell or electro-optic modulator to produce sidebands on the carrier signal. This carrier is given by the emission wavelength of the laser source. The laser beam is back-reflected from the optical resonator and detected with a high-speed photo-detector. On resonance this signal vanishes. However, out of resonance the sidebands can be observed, oscillating at the modulation frequency. Since these sideband waves are oscillating at a frequency that does not match the carrier frequency, the sidebands are totally reflected from the cavity. As one will see, these sidebands carry some phase-information of the position of the carrier wave in frequency space. That offers the possibility to distinguish whether the carrier is above or below resonance. The photo-detector signal picked up from the back-reflection is mixed<sup>10</sup> with the modulation signal to generate an error signal that has opposing signs above and below resonance. It is this signal that can be fed back to the laser source after some low-pass filtering to hold the cavity on resonance and to lock the laser frequency.

The primary aim in this work was to generate an intensity build-up within the resonator providing some enhancement of detection sensitivity for an eventual spectroscopic application (e.g. applications could be: cavity enhanced absorption spectroscopy (CEAS), cavity ring-down spectroscopy (CRDS), or intra-cavity quartz enhanced photoacoustic spectroscopy (I-QEPAS)). In a different application a stable laser frequency might be the primary aim. Of course both appears at the same time, and is a consequence of constructive interference of waves inside the resonator.

As shown in section 1.2.3 light can only pass an optical resonator if the frequency of an electromagnetic wave is an integer number of the free spectral range. The transmission of light is maximized if this condition is met. This leads to periodic

---

<sup>10</sup>Forming the product of the inputs

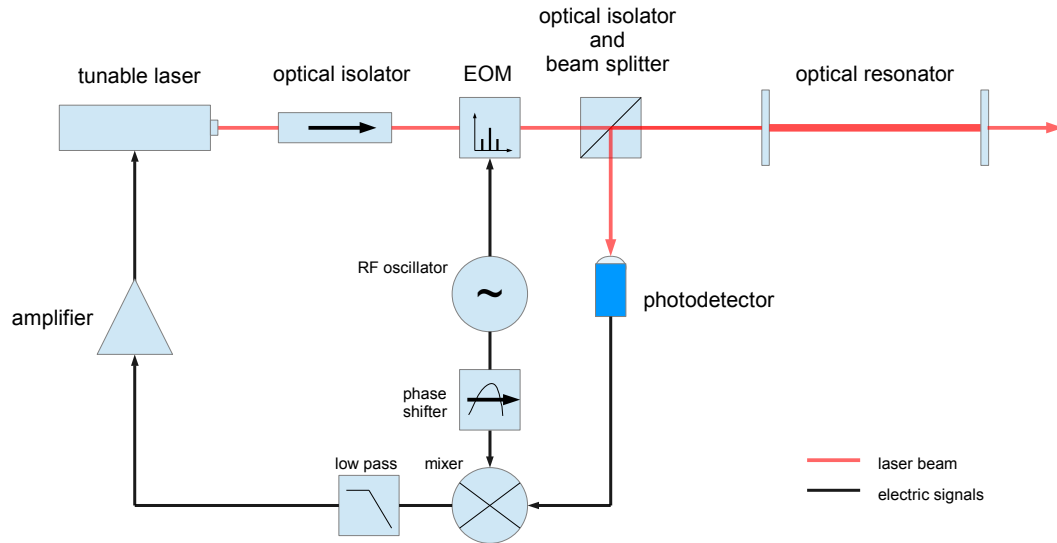


Figure 1.7: Basic setup of the PDH-system, based on [19]

transmission and no reflection in frequency space every free spectral range. Stabilizing the frequency of a laser could also be achieved by detecting the signal that is transmitted through the resonator; but in this case it is unknown if fluctuations of the detected signal are due to frequency drift or intensity changes of the laser beam. In order to decouple these two quantities, Drever et al. [20] suggested to measure the reflected signal.

The reflected intensity of a laser beam from a Fabry-Pérot resonator has the same periodicity as the transmission (consider  $T + R = 1$ ). It is symmetric in the vicinity of resonance, as shown in figure 1.8, leading to the fact that the value of the reflected power alone provides no information whether the laser frequency is below or above resonance, as one can see from the following: assume that the momentaneous laser frequency is slightly above resonance. If the frequency increases, the reflected power will also increase. Otherwise, if the frequency decreases, the reflected power will decrease. Below resonance this situation is inversed. However, the derivative of the reflected power provides the information needed. A positive change of the laser frequency above resonance will increase the reflected power, whereas below resonance, increasing the laser frequency will decrease the reflected power. In the

PDH-technique though this information is utilized by the phase of the reflected signal as will be shown in the subsequent.

If one considers an incident wave of frequency  $\omega$  arriving at the resonator  $E_{\text{inc}} = E_0 e^{i\omega t}$  and a reflected wave  $E_{\text{ref}} = E_1 e^{i\omega t}$  one can write the reflection coefficient of a lossless symmetric Fabry-Pérot cavity (see [19], p. 81), which is given by the amplitude-ratio of the incident and the reflected electromagnetic wave

$$F(\omega) = \frac{E_{\text{ref}}}{E_{\text{inc}}} = \frac{r(e^{i\frac{\omega}{\Delta\nu_{\text{FSR}}}} - 1)}{1 - r^2 e^{i\frac{\omega}{\Delta\nu_{\text{FSR}}}}} \quad (1.42)$$

with the amplitude reflection coefficient of the mirrors  $r$ . The angular frequency of the laser,  $\omega = 2\pi\nu$ , will be the carrier<sup>11</sup> frequency in the discussion following below. A plot of the squared absolute value of the reflection coefficient  $|F(\omega)|^2$  is shown in figure 1.8. For a monochromatic wave this quantity is equal to the reflected power. A mirror reflectivity of 0.9 was chosen to better visualize the characteristic. The phase of the reflection coefficient, given by  $\arg(F(\omega)) = \arctan(\frac{\text{Im}(F(\omega))}{\text{Re}(F(\omega))})$ , is shown in figure 1.9. It has a discontinuity on resonance and opposing signs below and above resonance, which is crucial for the PDH-technique.

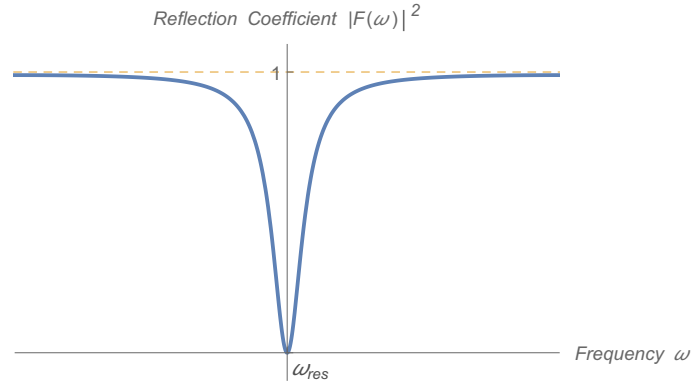


Figure 1.8: Reflection coefficient in the vicinity of resonance

The reflected beam is the sum of two beams. One part is reflected instantaneously, and another one is leaking out of the cavity. Exactly on resonance, those two beams interfere destructively and the signal vanishes. To make use of the phase information in the reflection coefficient, the PDH-technique is based on frequency modulation (or

<sup>11</sup>The carrier frequency  $\omega = 2\pi c/\lambda \approx 4.104 \times 10^{14}$  Hz is given by the QCL emission wavelength, which is  $\lambda = 4.59 \mu\text{m}$  for the employed QCL in this work.



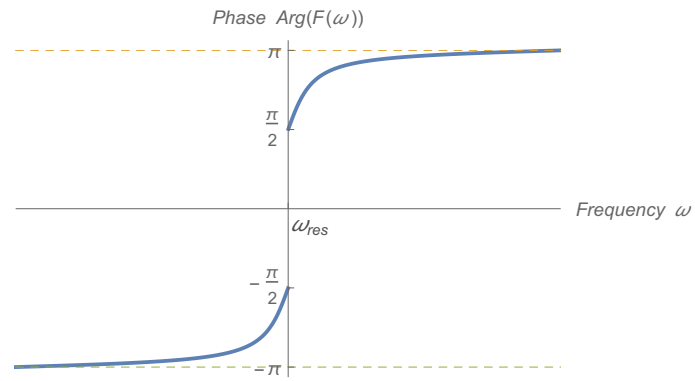


Figure 1.9: Phase of the reflection coefficient in the vicinity of resonance

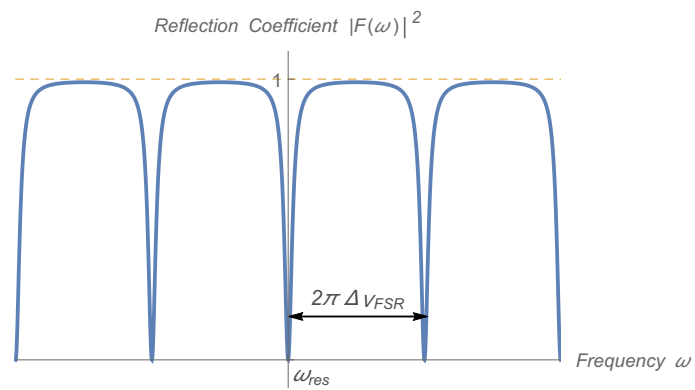


Figure 1.10: Reflection coefficient: evenly spacing in frequency space, separated by the FSR

equivalently phase modulation). If the laser frequency is modulated by an oscillator with a modulation frequency  $\Omega$  and modulation depth  $\beta$  described by

$$E_{\text{inc}} = E_0 e^{i(\omega t + \beta \sin(\Omega t))}, \quad (1.43)$$

the incident wave<sup>12</sup> can be approximated using a Taylor-series expansion or alternatively, as in [19], Bessel functions  $J_i(\beta)$  of order  $i$ . The resulting wave can be written

$$E_{\text{inc}} = E_0 [J_0(\beta) e^{i\omega t} + J_1(\beta) e^{i(\omega+\Omega)t} - J_1(\beta) e^{i(\omega-\Omega)t}], \quad (1.44)$$

and shows the presence of three waves: a carrier wave<sup>13</sup> oscillating with  $\omega$ , and two sidebands<sup>14</sup> oscillating with  $\omega \pm \Omega$ . It will be the sidebands that provide the phase information from the reflected signal.

To get a mathematical expression for the reflected signal, the incident modulated wave from equation (1.44) has to be multiplied in each term by the reflection coefficient evaluated at the corresponding frequency, leading to

$$E_{\text{ref}} = E_0 [F(\omega) J_0(\beta) e^{i\omega t} + F(\omega + \Omega) J_1(\beta) e^{i(\omega+\Omega)t} - F(\omega - \Omega) J_1(\beta) e^{i(\omega-\Omega)t}]. \quad (1.45)$$

Since the photo-detector can only measure the power in a laser beam, one has to calculate  $P_{\text{ref}} = |E_{\text{ref}}|^2 = E_{\text{ref}}^* E_{\text{ref}}$ , so that one ends up with the total reflected power  $P_{\text{ref}}$  (see [19], p. 82, eqn. 3.3) that arrives at the photo-detector

$$\begin{aligned} P_{\text{ref}} = & P_c |F(\omega)|^2 + P_s |F(\omega + \Omega)|^2 + P_s |F(\omega - \Omega)|^2 \\ & + 2\sqrt{P_c P_s} (\text{Re}[F(\omega) F^*(\omega + \Omega) - F^*(\omega) F(\omega - \Omega)] \cos(\Omega t) \\ & + \text{Im}[F(\omega) F^*(\omega + \Omega) - F^*(\omega) F(\omega - \Omega)] \sin(\Omega t)) \\ & + (2\Omega \text{ terms}) \end{aligned} \quad (1.46)$$

The first three terms of equation (1.46) are constant for a given carrier frequency  $\omega$  and modulation frequency  $\Omega$ , and therefore would only produce a DC signal on the detector<sup>15</sup>. The expressions of interest are the cosine-term and the sine-term, oscillating with the modulation frequency  $\Omega$ . These terms contain the phase infor-

<sup>12</sup>The total power of the incident wave is given by  $P_0 = |E_0|^2$

<sup>13</sup>The power in the carrier is given by  $P_c = J_0^2(\beta) P_0$

<sup>14</sup>The power in one sideband is given by  $P_s = J_1^2(\beta) P_0$

<sup>15</sup>Technically it depends on the pre-amplifier of a photo-detector if a DC signal is visible. In most cases it is not. This also applies to the utilized photo-detectors in this work.

mation of the carrier wave. At high modulation frequencies, i.e.  $\Omega \gg \frac{2\pi\Delta\nu_{\text{FSR}}}{\text{Finesse}}$ , only the sine-term is important, and the cosine-term vanishes [19].

This signal is fed into one input of the mixer and multiplied by modulation-signal that is fed into the second input. The product of two sinusoidal signals, that oscillate with different frequencies, is given by

$$\sin(\Omega t)\sin(\Omega' t) = \frac{1}{2}[\cos[(\Omega - \Omega')t] - \cos[(\Omega + \Omega')t]]. \quad (1.47)$$

Therefore, if  $\Omega = \Omega'$ , and additionally, the phase of the modulated signal is manipulated by the phase-shifter to match the phase of the detector signal, the output of the mixer will contain a DC-part from  $\cos[(\Omega - \Omega')t]$ , and a fast oscillating part from  $\cos[(\Omega + \Omega')t]$ . Since the output-signal from the mixer is subsequently filtered by a low-pass filter, only the DC-part remains, and one finally ends up with an appropriate error-signal that can be fed back to the laser-source.

For high modulation frequency (as defined above) this error-signal [19] is given by equation (1.48)

$$\epsilon = 2\sqrt{P_c P_s}(\text{Im}[F(\omega)F^*(\omega + \Omega) - F^*(\omega)F(\omega - \Omega)]) \quad (1.48)$$

which is plotted in arbitrary units in figure (1.11). As one can see the reflected signal

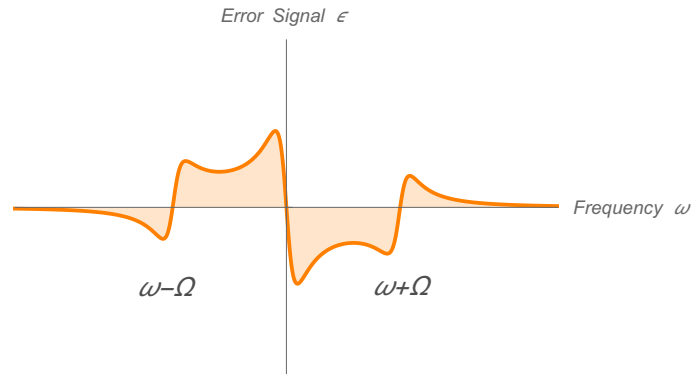


Figure 1.11: PDH error-signal

is zero on resonance<sup>16</sup> (located at  $\omega = 0$ ) and has a steep slope around resonance with opposing signs, which is the essence of the PDH-technique.

<sup>16</sup>The center of this signal where  $\omega = 0$  corresponds to any integer multiple of the FSR that is added to the cavity's resonance frequency

## Chapter 2

# Experimental Setup and Investigations

In this section the experimental setup is described, as well as the development of the system throughout the course of this work. The mode linewidth of a high-finesse optical resonator can be extremely narrow depending on the finesse and cavity length. The need of a low noise laser system basically arises from this fact. It might be intuitively clear that any noise within the system could have adverse effects on the laser signal, and consequently could lead to a broadening of the laser linewidth. As one will see in the final chapter the laser linewidth is a very critical parameter when injecting laser light into a high-finesse optical cavity, and is strongly influenced from noise. Therefore, one of the major tasks in this work was the investigation of noise-sources within the setup and the laboratory, as well as grounding and shielding measures together with signal filtering.

The original setup from Drever et al. [20] was adopted with some suggestions of Black [19], and applied to the domain of QCLs with todays offerings of the mid-IR market. The technical equipment is described in section 2.2 to get an overview about the used components. Hints and investigations that were made during the setup of the system are included regarding these components. The laser beam alignment is then described, as this might not always be straight-forward, especially when aligning the cavity mirrors. The mode-matching parameters are calculated in a separate detailed section following in the subsequent. A short, theoretic section about the influence of some cavity parameters on the PDH error signal shall visualize some given correlations. Different types of noise are described, and some counter-measures are

proposed that were later applied in this work. The attained improvement of noise performance is then presented before, in the end of this chapter, some experimental approaches are described.

## 2.1 Basic Experimental Setup

The setup presented in section [1.3 Pound-Drever-Hall \(PDH\) Laser Frequency Stabilization](#) was adopted in a way that is visualized in figure [2.1](#). As to the author's knowledge and at the time of writing there was no electro-optic modulator operating in the mid-IR commercially available. Therefore, the frequency modulation for generating the sidebands had to be fed directly into the laser driver. As turned out, this had, from a noise performance point of view, adverse effects because additional noise was introduced to the driver by this connection. Moreover, this led to a different approach than in the original setup: when the phase of the laser beam is modulated with some electro-optic modulator the intensity of the beam is not influenced. This is in contrast to the current-modulation applied in this work because the output power of the laser depends on the current. If one adds a sinusoidal signal onto the carrier-wave, for generating frequency modulation (FM), this leads to a periodic change of the beam intensity which may have unwanted effects depending on the modulation depth.

A more detailed drawing of the final PDH-setup is provided by figure [2.2](#). Here the whole system is shown as it was built up in the lab. A photograph where most of the used components are depicted is given in the [Appendix](#). An optical bench supported by an active suspension to attenuate vibrations was used. The single components of the setup are described in detail in the following section [2.2 about Technical Equipment](#). For practical purposes a right handed coordinate system shall now be introduced: the laser beam direction is denoted as the z-direction. Transverse directions are given by x and y. This means that the x-z plane is parallel to the bench. The laser beam emitted by the CW-DFB-QCL was spatially filtered by a telescope configuration, consisting of a 100 mm lens, a pinhole and a 40 mm lens. The beam then propagated through the Faraday isolator, a polarizer and a wave-plate. Afterwards, the beam was deflected in the x-z plane with an adjustable gold-coated mirror, passed through the 500 mm mode-matching lens and was again deflected in the x-z plane by another gold-coated mirror. Finally, the beam hit the cavity entrance mirror.



The detection of its back-reflection was achieved by a high-speed photo-detector. The acquired signal was fed into the control electronics (main in), which internally applied the signal processing, i.e. mixing, filtering and phase-shifting as described in section 1.3. The QCL driver as well as the TEC controllers were powered by batteries. The scan control and the modulation output of the electronics unit were connected directly to the driver via some filtering circuits. All signal connections were made up of shielded BNC cables and connectors, except for the connection between TEC 1 and the QCL protection circuit, as well as the connection from the laser driver to the QCL protection circuit. These connections were realized with triaxial cables and connectors (cable: Belden 9222, connectors: Pomona). The cavity mirrors, the 40 mm lens, the pinhole (spatial filter), the 500 mm lens and the Faraday isolator were mounted on linear micrometer stages with the possibility of full x-y-z adjustment. In addition, the cavity mirrors were held by a kinematic mirror mount with two tilt-able axes for aligning purposes. The two gold-coated mirrors were mounted on kinematic mirror mounts, offering the possibility of perpendicular alignment of the laser beam with respect to the cavity axis. During the setup the signal from the photo-detector was investigated with an oscilloscope in the time-domain, and with a spectrum analyzer in the frequency-domain. The latter was valuable for the investigation of noise.

## 2.2 Technical Equipment

In this section the technical equipment is described in some detail. Therefore, if reasonable, a few anticipations are made that will be treated in the sections following below. This particularly applies to components that were involved in issues with electronic noise.

**Laser Source** A continuous-wave distributed feedback quantum cascade laser (CW-DFB-QCL, AdTech optics, model HHL-14-15) with a center-wavelength of  $4.59\ \mu\text{m}$  and a maximum power output of 47.5 mW at 25 °C was utilized. The current wavelength tuning factor was determined in a separate work to be  $-0.6\ \text{cm}^{-1}/40\ \text{mA}$ , which has good coincidence with the datasheet value of 30 nm/A. The temperature wavelength tuning factor is 41 nm/K. The beam characteristics provided from the manufacturer are summarized in the following table:

optical planes	lateral	vertical	unit
full beam waist	3.05	3.68	mm
beam waist location	1179.7	1651.4	mm
divergence angle	0.96	0.79	mrad
$M^2$ (beam quality factor)	1.13	1.22	-

**Laser Protection Circuit** Quantum cascade lasers are very sensitive devices that can easily be damaged or destroyed by electrostatic discharge (ESD), unallowable high currents or temperatures, and reverse bias. In order to sustain the vitality of the laser-source a protection circuit was built up with a special commercially available protection diode (Lasorb), in combination with a transil-diode and a quartz-sand filled fuse. The protection-diodes were placed in parallel to the QCL's terminals in a reverse direction. The fuse was placed within the positive supply line. To point out, there might be a significant voltage-drop across fuses, due to their typical resistance of a few ohms, which might be considered as an additional load for the laser-driver. This particular circuit protected the laser from ESD-pulses, unallowable high currents and reverse bias. The temperature was supervised and controlled by a thermo-electrical controller (TEC) (see section 2.2). The unshielded protection circuit that was used in the beginning, originated from a previous setup; it most likely picked up common mode noise from switching elements and coils of a TEC that had also been previously used; it was consequently substituted by a linear TEC later on in this work. Since high-frequency (HF) noise from the environment and from the TEC strongly coupled onto the laser-output signal via this path of the unshielded protection circuit, it was shielded with a fully closed aluminum die-cast housing, and directly plugged onto the pins of the QCL HHL-housing (high heat load) by a pin-connector. The housing was equipped with three female triaxial-connectors. One to connect to the laser-driver output, and two connections going to the TEC for the connection of a NTC (negative temperature coefficient) sensor and the TEC current output. Finally, one can say, it is a safe and low-noise approach to have a shielded housing for any laser protection-circuit.

**Thermo-Electrical Controller (TEC)** Laser diodes as well as QCLs need active cooling during operation. A TEC is capable of driving a Peltier-element by measuring the temperature in the vicinity of the laser via, e.g. a NTC-sensor, and providing PID (proportional integral derivative) control of a current that is fed into the Peltier-



element by an electronic feedback loop to reach a specified temperature setpoint. The initial setup included a TEC with noisy switching elements and coils. Obviously the steep rise and fall time of the TEC-current signal coupled onto the laser signal; it was directly visible with the photo-detector in a simple experiment. After replacing this controller with a linear TEC (Wavelength Electronics, PTC2.5K-CH) this noise source vanished. As from the datasheet, this particular TEC offers a long term temperature stability of 0.002 K (24 h) and a short term temperature stability of 0.0012 K (1 h). It was connected to the HHL housing of the laser via the protection circuit (triaxial-cable) and powered by a 24 V battery as a low-noise power supply. A second, identical TEC was used to control the temperature of the laser housing.

**Custom-Made Prototype of a Low-Noise CW-QCL Driver** A custom-made laser driver<sup>1</sup> prototype was used from the start as a low-noise current source to operate the QCL. It was based on 4-layer SMT board, and equipped with a modulation input and a scan-input, which was a requirement for the use with the control electronics, i.e. the frequency stabilizer (Digilock 110). This prototype was still under development while this work was going on. The functionality and noise performance of this device was of great importance for the success of this work. First, the performance of the laser-driver was investigated with a 50  $\Omega$  power-resistor and a spectrum analyzer; this particular value for the resistor was chosen to simulate an equivalent but resistive load to the driver, as provided by the QCL, which is of capacitive [12] load. After safe operation was approved, the laser driver was connected to the QCL. It was integrated in a full aluminum die-cast housing for shielding purposes, equipped with a triaxial connector for the connection to the QCL, and placed on top of the aluminum 19 inch rack containing the battery power supply. Finally, the development of this laser-driver stopped because the person in charge left the institute. The device remained in an early stage of development and was still suffering from some technical issues. Therefore a commercial alternative had to be found.

**Commercial Low-Noise CW-QCL Driver** The QCL1000 manufactured by Wavelength Electronics is a low-noise current source for driving a QCL. It features an average noise current density of 2 nA/ $\sqrt{\text{Hz}}$  and a RMS noise current of 0.7  $\mu\text{A}_{\text{RMS}}$  in a 100 kHz bandwidth. This laser driver was employed in the ongoing work. The results obtained are based on this device.

---

<sup>1</sup>Developed in a separate work at the Institute of Chemical Technologies and Analytics at Vienna University of Technology; not published yet

**Battery Power Supplies** Since it is a good strategy to diminish noise and ripple at the source, the use of a battery power supply for the QCL was considered and built up, serving as a low-noise and independent power source. A 19 inch full aluminum rack provided a housing for two 24 V batteries. The laser driver had to be powered with a symmetric power supply of +24/0/-24 V. In order to provide these voltages, two rechargeable valve regulated lead acid batteries (each of 7 Ah power capacity), suitable for an uninterruptible power supply, were connected in series. Two separate charging devices were connected to each of the batteries to avoid the need of additional battery balancing that would have been necessary if a single charging device with the double voltage had been used. A switch was mounted at the outside of the housing to select between 3 states: charge, off and laser power on. A three-pole main power connector with included line filter was attached on the backside of the housing. This connection is intended to be only needed while charging the batteries, and it should be disconnected during laser-operation in order to minimize noise. Since usually battery voltage falls off with decreasing charge, and because the actual voltage of the batteries was approximately 27.6 V at full charge, therefore exceeding the electric power input specifications of the utilized driver, a heat-sinked voltage regulator circuit was built up in order to not overload the laser driver (QCL 1000, max. input voltage 25 V). An output voltage of 24 V was realized by use of voltage regulators (LM317 for the positive supply line, LM337 for the negative supply line). In a first approach only the laser driver was powered by batteries. To improve the system noise performance the TEC was powered by a single 24 V battery as well, and mounted in a separate 19 inch full aluminum rack.

**Photo-Detectors** For the detection of the back-reflected error signal a VIGO System detector (model PVMI-4TE-8) was used. It is a photovoltaic, multiple junction MCT detector operating at a temperature of 194 K. It is equipped with an integrated TEC and a pre-amplifier. The detector element has an active area of  $1 \times 1$  mm separated from the environment by a wedged  $\text{BaF}_2$ -window. The pre-amplifier has a low-cutoff frequency of 5 kHz and a high-cutoff frequency of 250 MHz. The specific detectivity ( $\pm 20\%$  at  $\lambda = 8 \mu\text{m}$ ) is  $D^* = 1.5 \times 10^9 \text{ cm}\sqrt{\text{Hz}}/\text{W}$  and the corresponding output voltage responsivity is 2.15 mV/W. The averaged output noise density is 140 nA/ $\sqrt{\text{Hz}}$ .

The transmission signal of the cavity was investigated with a  $\text{LN}_2$ -cooled MCT-detector (Infrared Associates, model FTIR-16-2.00) that offers a higher detectivity

of  $D^* > 2.0 \times 10^{10} \text{ cm}\sqrt{\text{Hz}}/\text{W}$  and is able to detect signals from almost DC up to multiple kHz.

**Optical Isolator** The optical isolator was placed between the laser and the resonator. The necessity of an optical isolator in the PDH setup is justified by protecting the laser from destabilization or damage due to back-reflections from the cavity mirrors. The functionality of the used isolator in this work is based on the Faraday-effect: the plane of polarization of the incident laser beam is rotated by a strong magnetic field from a permanent magnet after the beam has passed a vertical polarizer. After being rotated by the Faraday-rotator, a second polarizer (called analyzer) only permits passing light in its main axis of polarization. Light that travels backwards through the optical isolator, first passes the analyzer and gets then rotated again in the same direction as the incident wave. It is therefore completely canceled out by the input polarizer leading to the diode-like behavior of an optical isolator. After the beam leaves the isolator, the polarization axis is rotated clockwise by  $45^\circ$  when looking in forward direction. The optical isolator used in the setup (eotech, [32]) has a transmission of around 68 %, and offers an isolation of the reverse beam intensity of around 34 dB at the according wavelength of 4600 nm.

**Polarizer and Quarter Wave-Plate** After passing the optical isolator the laser beam is linearly polarized. A polarizer is an optical element that only permits the passage of linear polarized light, while it attenuates waves of random or orthogonal polarization. First the beam hits the polarizer, which is tilted horizontally in the plane of the bench by  $45^\circ$  to operate as a beam-splitter for the back-reflected signal, and to route it onto the photo-detector. The polarization axis of the polarizer therefore has to be coincident with the output polarization of the beam after passing the optical isolator. After passage of the polarizer, the beam hits the quarter wave-plate. It generates circular polarization by an introduced phase shift to the polarization-vector components of the incident field. This is achieved if the optical axis of the quarter wave-plate is rotated by  $45^\circ$  with respect to the incident polarization. Other rotation angles would lead to elliptic polarization. With now the beam being circularly polarized it enters the cavity. After the beam returns from the cavity mirrors it still is circularly polarized when it passes the quarter wave-plate; now the process is reversed, and the beam gets linearly polarized again, ending up with orthogonal polarization with respect to the polarizer's axis. Consequently, the beam is attenuated by the

polarizer, and the reflection from its surface is picked up with the photo detector. To summarize that: the combination of the polarizer and the quarter wave-plate works as a beam splitter and optical isolator. The mid-IR polarizer used in this work was a holographic wire grid polarizer on a  $\text{CaF}_2$  substrate (Thorlabs). The mid-IR quarter-waveplate (Altechna) is AR-coated on both sides; the center wavelength of operation is 4500 nm, and offers a transmission coefficient of  $T \approx 0.5$  at 4600 nm.

**Curved High-Reflectivity (HR) mid-IR Dielectrically Coated Mirrors** The mirrors originating from CRD-optics [31] had a reflectivity of  $R = 0.9998$ , and usually find their application in cavity ring-down spectroscopy (CRDS). The center wavelength of maximum reflectivity was 4600 nm. The diameter was 0.8 inch at a thickness of 0.635 cm. The radius of curvature was specified as 1 m. However, a simple experiment uncovered that the actual radius of these mirrors was rather 6 m. The curved side had an HR-coating, whereas the flat side has an AR-coating (anti reflective). The bulk material was ZnSe, which has a refractive index of  $n = 2.431$  at  $4.59 \mu\text{m}$  wavelength [33]. Of course this high reflectivity is only reached if the surface is not contaminated. Careful cleaning with lens tissue and acetone was done before mounting the mirrors.

**Mode-Matching Lens** The lens for matching of the beam's RoC to the cavity's RoC at the boundary surface, and consequent excitation of the resonators Gaussian modes, was a conventional  $\text{CaF}_2$  plano-convex lens with a high transmission in the mid-IR; the diameter was 25.4 mm and the focal length  $f = 500$  mm. The calculation of its required position in the beam path is carried out in section 2.3.2.

**Electronics and Digital Control** To control the laser frequency a commercially available FPGA-based feedback control device, running a LabVIEW environment, was used (Digilock 110, Toptica Photonics, [34]). It features 21-bit resolution for the frequency scan control of the laser and offers different PDH modulation frequencies (1.56 MHz to 25 MHz). Possible scan frequencies range from  $0 - 10^4$  Hz with a triangular scanning ramp waveform. An integrated auto-lock mode based on two fully configurable PID-controllers provided the PDH functionality needed. Some modifications were made: the laser scan control of the Digilock 110 is designated to be connected to a separately available module at the backplane (SC110, scan control). The output at the front plate of the device only provided a scan resolution

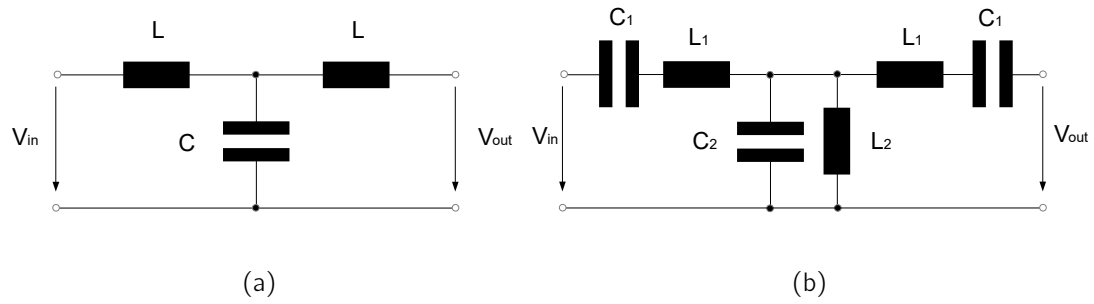


Figure 2.3: Passive electronic filters of 3<sup>rd</sup> order (a) *LC* low-pass (b) *LC* band-pass

of 14 bit. Therefore a standard DIN 96-pin connector was attached to the backplane connection to get use of the full 21 bit resolution; the output pin for the scan control (SC110 out, 21 bit) was soldered to a BNC cable, and connected to the analog input of the laser driver.

**Electronic Filters** Due to the recognition of noise transmitted over the signal paths between the electrical control unit (Digilock 110) and the laser driver electrical filtering was necessary. Different approaches, covering active filters as well as passive filters, finally led to the following choices: the signal path (BNC cable) between the scan control output of the Digilock and the laser driver's analog input was filtered with a passive *LC* T-shape low-pass filter of 3<sup>rd</sup> order (figure 2.3 a) with a cutoff-frequency (-3 dB) at 5 kHz. Additionally, open-able ferrite core rings for suppression of electromagnetic interference (EMI) were attached on the BNC cables for further noise improvement, showing effectivity especially in the higher frequency domain above several MHz. The signal path between the Digilock (main out), for the transmission of the modulation signal, was filtered with a *LC* T-shape band-pass of 3<sup>rd</sup> order (figure 2.3 b) with a center frequency of 1.6 MHz and a band-pass gap of 0.5 MHz. The components (capacitors and coils) were selected with focus on low tolerances; in the case of coils the frequency response was taken into account to effectively filter out higher frequency components, since coils usually show a lower impedance at higher frequencies due to parasitic parallel capacitance. Each of the filter circuits were soldered on a printed circuit board and mounted in a small fully enclosed aluminum die-cast housing (shield) that had BNC-connectors attached. The functionality of these filters was examined by a check of the filter response; the signal from a function generator was fed into the filter circuit, and the response was measured with an oscilloscope.

## 2.3 Laser Beam Alignment and Cavity Setup

The whole system was built up sequentially. First of all, the laser beam was aligned parallel to the bench. This was done by measuring the height of the beam-output of the laser with respect to the bench (105.0 mm) using an IR-CCD camera (Spiricon Pyrocam III) that provided live-view of the lasers beam profile on a monitor screen. It was compared to the lasers target point at the very end of the bench; the angular shift was then corrected directly at the mounting of the laser source. The alignment procedure described in the following in principle applies to every additional component added to the beam path. The camera is placed in the beam-path further away from the point where a new component shall be placed, and the position of the laser beam targeting the CCD-chip of the camera is marked on the monitor screen. The new optical component (e.g. lens, optical isolator, etc.) is then placed at a designated position. It is moved in a transverse plane, and if necessary, tilted in a way to pan the laser beam back onto the initial point on the monitor screen before the component was added. This ensures the conservation of a strictly linear beam-path after every additional component. To eliminate multiple reflections of the laser beam between optical elements, and to avoid back-reflections into the laser-source, every component was tilted slightly. This of course, was not applied to the cavity's mirrors. In order to appropriately fit the laser beam through the optical isolator, without additional spatial attenuation by its aperture, a configuration of two lenses was utilized; a plano-convex lens with  $f = 100$  mm and another one with  $f = 40$  mm were positioned in a telescope configuration to reduce the beam diameter for this purpose. A pinhole with  $300\text{ }\mu\text{m}$  diameter was placed at the overlapping focal points of this lens-configuration in order to work as a spatial filter, and to reach an almost perfect Gaussian beam profile. Subsequently the optical isolator was placed in the beam-path, and it was ensured not to cut off the laser beam in its transverse direction by the introduced aperture. The following element in the PDH setup was a polarizer, working as a beam-splitter to route the back-reflected laser beam onto the IR-detector. This was achieved by tilting the polarizer  $45^\circ$  in a plane parallel to the bench with respect to the incident beam. Care was taken to rotate the polarizer in a way to align the optical axis  $45^\circ$  with respect to the beam-axis because the laser beam was polarized in the same direction after it passed the optical isolator. As a next component the  $\lambda/4$ -wave-plate was placed; its optical axis was aligned perpendicular to the bench in order to circularly polarize the incident beam. Because of issues with the available space on the optical bench a gold-coated mirror was

added as a next component to deflect the beam by  $90^\circ$  in the x-z plane further on to the mode-matching lens. The mode-matching lens with 500 mm focal length was placed at the calculated position on a x-y-z linear micrometer-stage; here again, as for any other optical component, it was necessary to work with the IR-camera to align the mode-matching lens in a way to compensate for misalignment in the transverse direction. Another mirror was placed afterwards to deflect the beam once again in order to guide it onto the cavity mirrors. Subsequently the cavity mirror being farther away from the source was placed in the beam-path using a kinematic mirror mount, which was tilt-able in two independent directions and attached on a fully x-y-z adjustable linear slider to have superior control throughout the alignment process. Specially customized adapter rings were manufactured in house to perfectly fit the mirrors into the kinematic mirror mounts, providing the accuracy needed for aligning the cavity mirrors. The mirror being farther away from the laser-source was aligned by shifting the mirror in x-y direction so that the laser beam hit the center of the curved mirror-surface. At this point it is crucial to have a reference for aligning both cavity mirrors with respect to each other to achieve collinear back-reflection of the beam, which is a necessary condition for the emergence of constructive interference. Hence two adjustable iris diaphragms were added into the interspace between the two mirror positions. The beam was aligned by altering the angular shift of the beam with both gold-plated mirrors by means of their kinematic mountings to ensure that the beam was passing linearly through both iris diaphragms. The aperture of the iris diaphragm was continuously minimized for fine-adjustment of this alignment. Then the reflected beam was visualized with the IR-camera, which was positioned instead of (and at the usual position of) the photo-detector during the alignment procedure; the x-y position of the beam targeting the CCD-chip was marked on the monitor screen. Finally, the second mirror (front mirror) was added into the beam path. Now the front mirror was tilted to bring the reflection back to coincidence with the previously marked point on the monitor screen stemming from the cavity's rear mirror. After these steps the alignment process of the cavity was complete.

### 2.3.1 Cavity Parameters

The cavity parameters can be summarized as follows: the reflectivity of the mirrors  $R = 0.9998$  leads to a finesse of around  $\mathcal{F} = 15706$  (equation 1.31). The free spectral range for the experimental standard cavity length of 1 m is around  $\nu_{\text{FSR}} = 150$  MHz (equation 1.30). The corresponding cavity mode linewidth  $\Delta\nu = 9543$  Hz

(equation 1.32). The cavity's decay time (ring-up time, photon life-time) is around  $\tau_p = 16.7 \mu s$  (equation 1.35) and the waist radius  $W_0 = 1557 \mu m$  (equation 1.40). In figure 2.4 these parameters are summarized for different resonator lengths. Figure

length / m	FSR / Hz	decay time / s	linewidth / Hz	waist radius $w_0$ / $\mu m$
0,05	2,997925e+09	8,339e-07	190854	751
0,10	1,498962e+09	1,668e-06	95427	893
0,20	7,494811e+08	3,336e-06	47713	1059
0,30	4,996541e+08	5,003e-06	31809	1170
0,50	2,997925e+08	8,339e-06	19085	1324
0,75	1,998616e+08	1,251e-05	12724	1457
1,00	1,498962e+08	1,668e-05	9543	1557
1,25	1,199170e+08	2,085e-05	7634	1636
1,50	9,993082e+07	2,502e-05	6362	1703
2,00	7,494811e+07	3,336e-05	4771	1807
2,50	5,995849e+07	4,170e-05	3817	1887
3,00	4,996541e+07	5,003e-05	3181	1948
4,00	3,747406e+07	6,671e-05	2386	2033
5,00	2,997925e+07	8,339e-05	1909	2079
6,00	2,498687e+07	1,001e-04	1591	undefined

Figure 2.4: cavity parameters

2.5 (a) shows the influence of the resonator length on the ring-up time. As one will see in the final chapter this is a very critical parameter for producing resonance. For comparison a mirror reflectivity of 0.999 is shown. As one can see, the ring-up time for a cavity with a lower finesse is decreased. This is a consequence of the lower bounce number of the photons on average, before they leave the resonator. In figure 2.5 (b) the linewidth is plotted in dependency of the resonator length for two different mirror reflectivities. The linewidth decreases with increasing resonator length. In general, the linewidth of a lower finesse cavity is larger, indicated by the lower slope of the corresponding line. Plot 2.5 (a) and (b) have an inverse relationship with respect to each other described by equation (1.35). It is worth to mention that the cavity's linewidth can be drastically broadened by reducing the resonator length as one can see from figure 2.5 (b). Figure 2.6 (a) shows the cavity's beam waist radius according to equation (1.40); it is plotted for three different mirror radii. The uppermost blue line indicates the realization in the experiments. One can see that a decreased mirror radius of curvature causes in general a smaller beam



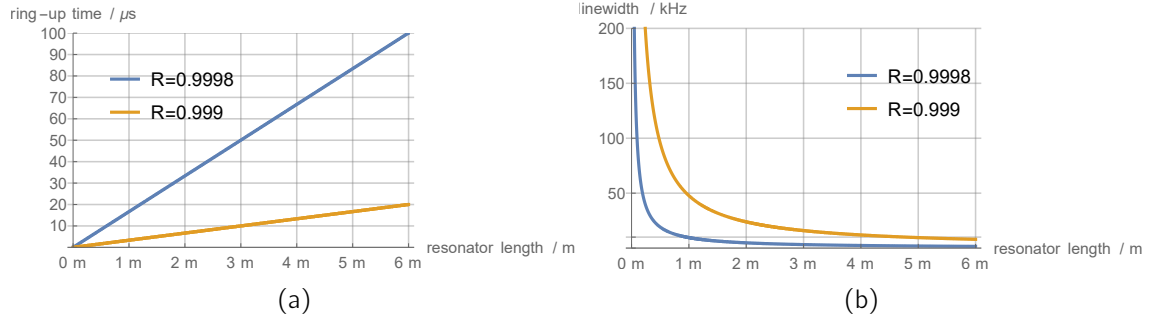


Figure 2.5: Influence of resonator length  $L$  on (a) on ring-up time  $\tau_p$  (b) cavity mode linewidth  $\Delta\nu$  for two different mirror reflectivities

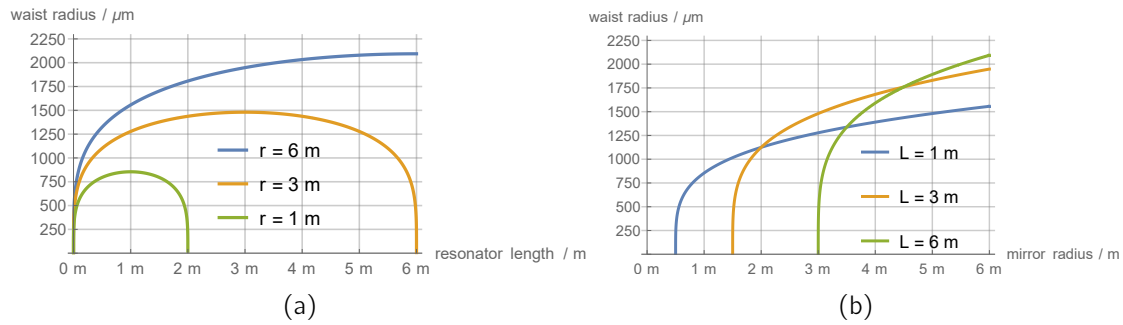


Figure 2.6: (a) Influence of resonator length  $L$  on intra-cavity beam waist radius  $W_0$  for three different mirror radii  $r$ , and in turn (b) influence of mirror radius  $r$  on intra-cavity beam waist radius  $W_0$  for three different resonator lengths  $L$

waist; this might be of interest for certain spectroscopic applications. Due to the stability criterion from equation (1.38) the confinement condition  $0 \leq L \leq 2|r|$  for a symmetric resonator (i.e. equal mirror radii  $r_1 = r_2$ ) can be recognized. The cavity's beam waist will be important in terms of mode-matching.

### 2.3.2 Mode-matching Calculation

Referring to section 1.2.4, mode-matching of an optical resonator by use of one lens is shown in the following. For a proper calculation the position of the beam waist as a starting point had to be known. The determination of the beam waist was achieved by use of the IR-camera, and by support of its delivered software. The camera was placed at a certain distance apart from the 40 mm lens (in figure 2.2) within them beams z-direction. The  $1/e^2$  value of the beam diameter<sup>2</sup> was continuously measured, averaged and plotted in a live-chart; the lens was shifted in z-direction to find

<sup>2</sup>Where the beam-intensity of the center drops to  $1/e^2 \approx 0.135$

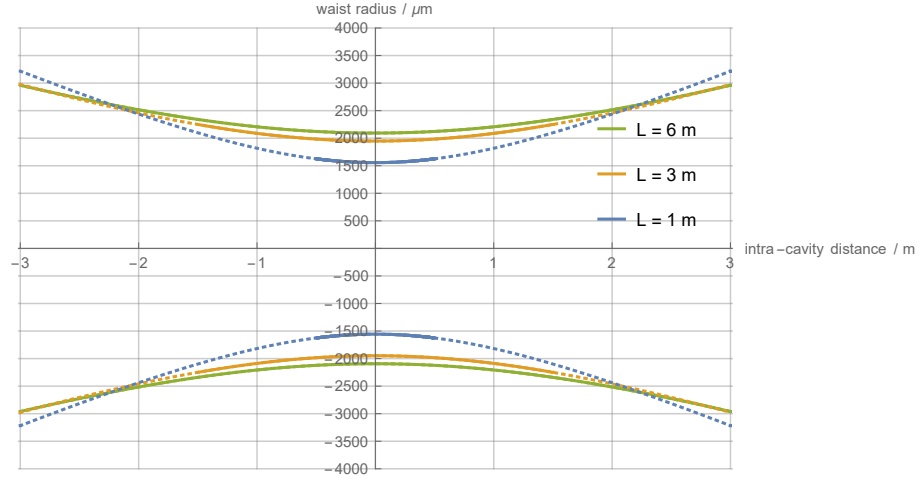


Figure 2.7: Comparison of the evolving Gaussian beam for three different cavity lengths  $L$  within the symmetric, spherical mirror resonator that has a mirror radius of  $r = 6$  m:  $L = 1$  m was realized in experiments (mirrors at  $\pm 0.5$  m),  $L = 3$  m corresponds to the concentric resonator (mirrors at  $\pm 1.5$  m),  $L = 6$  m corresponds to the confocal resonator (mirrors at  $\pm 3$  m). The dotted lines correspond to a virtual beam envelope beyond the resonator length; the beam waist is located at the origin.

the minimal waist. Consequently, the beam waist is located in the x-y plane of the CCD-chip's camera. Obviously in this case the lens was moved to minimize the laser waist diameter projected onto the CCD-chip. Therefore one can choose the position of the beam waist in advance by appropriate prior positioning of the camera, which is very convenient.

With the knowledge of the exact position and diameter of the beam waist the calculation starts with free space propagation by the distance  $d_1$  in air with refractive index  $n_1$ , from the determined beam waist to the mode-matching lens, i.e.

$$M_1 = \begin{pmatrix} 1 & d_1/n_1 \\ 0 & 1 \end{pmatrix}.$$

The convex mode-matching lens with focal length  $f$  is introduced by

$$M_2 = \begin{pmatrix} 1 & 0 \\ -1/f & 1 \end{pmatrix}.$$

Again it follows free space propagation by the distance  $d_2$  in air with refractive index  $n_1$ , from the mode-matching lens to the entrance-mirror of the cavity, i.e.

$$M_3 = \begin{pmatrix} 1 & d_2/n_1 \\ 0 & 1 \end{pmatrix}.$$

The following three matrices  $M_4, M_5, M_6$  describe the plane-concave cavity mirror with radius  $R$ , refractive index of the ZnSe-mirror  $n_2$  and of air  $n_1$ , and the mirror thickness  $s$ .

The transition from free space through the flat entrance-surface of the cavity mirror is described by the unity matrix

$$M_4 = \begin{pmatrix} 1 & 0 \\ \frac{n_1-n_2}{R} & 1 \end{pmatrix} \approx \begin{pmatrix} 1 & 0 \\ 0 & 1 \end{pmatrix}, \text{ for } R \rightarrow \infty.$$

The space propagation within the cavity mirror, with refractive index  $n_2$ , towards the curved surface over the distance  $s$ , representing the mirror thickness, is described by

$$M_5 = \begin{pmatrix} 1 & s/n_2 \\ 0 & 1 \end{pmatrix}.$$

The refraction of the beam at the curved boundary surface of the mirror with radius  $R$  is described by<sup>3</sup>

$$M_4 = \begin{pmatrix} 1 & 0 \\ \frac{n_2-n_1}{R} & 1 \end{pmatrix}.$$

Finally, the beam propagates in free space to the center of the optical resonator, where the cavity's beam waist is located, i.e.

$$M_7 = \begin{pmatrix} 1 & L/2 \\ 0 & 1 \end{pmatrix}.$$

The ray-transfer matrix of the total system is then

$$M_{ABCD} = M_7 M_6 M_5 M_4 M_3 M_2 M_1 = \begin{pmatrix} A & B \\ C & D \end{pmatrix}$$

Since the resulting matrix is quite large, its explicit form shall only be given in the [Appendix](#). The calculation was carried out by use of some computational mathematics

---

<sup>3</sup>One has to pay attention here to the reversed order of the refractive indices  $n_i$

software. The code is also provided in the [Appendix](#).

$$q_2 = \frac{Aq_1 + B}{Cq_1 + D} \quad (2.1)$$

Equation (2.1) has to be solved for the distances  $d_1$  and  $d_2$ . However, only real solutions of this complex equation are of physical relevance; by rearrangement of equation (2.1) one obtains equation (2.2). This form motivates that real solutions only exist, if the imaginary part vanishes

$$A \left( \frac{W_1}{W_2} \right)^2 - D - i \underbrace{\left( B \frac{\lambda}{\pi W_2^2} + C \frac{\pi W_1^2}{\lambda} \right)}_{=0} = 0. \quad (2.2)$$

This leads to a system of two equations (2.3), which provides real solutions for  $d_1$  and  $d_2$  (compare [17], p. 286)

$$\begin{aligned} A - D \left( \frac{W_2}{W_1} \right)^2 &= 0 \\ B + C \left( \frac{\pi W_2}{\lambda} \right)^2 &= 0. \end{aligned} \quad (2.3)$$

This procedure is iterative because not every combination of input parameters such as incident waist size, focal length of the lens or cavity length leads to useful results; negative solutions have to be dismissed, and in this case the input parameters have to be changed.

For a measured incident waist radius of  $w_i = 397.5 \mu\text{m}$  the table in figure 2.8 shows some calculated distances  $d_1$  and  $d_2$  for a set of different cavity lengths<sup>4</sup>.

## 2.4 Influence of Cavity Parameters on the PDH Error Signal

The influence of some cavity parameters, in particular the mirror reflectivity  $R$ , the cavity length  $L$ , and the modulation frequency  $\Omega$ , shall now be investigated with some plots of the PDH error signal given by equation (1.48). The plot in figure 2.9 (a) corresponds to the actual values used in the experiment. As one can read off from these plots by comparison, the error signal does not show the steep slope

---

<sup>4</sup>  $L = 3000 \text{ mm}$  corresponds to the concentric resonator,  $L = 6000 \text{ mm}$  to the confocal resonator

$L / \text{mm}$	$f / \text{mm}$	$d_1 / \text{mm}$	$d_2 / \text{mm}$	$w_0 / \mu\text{m}$
100	500	700,0	1348,8	892,7
500	500	624,6	1137,8	1323,5
1000	500	606,4	790,7	1556,6
1500	500	601,6	521,3	1702,7
2000	500	601,6	314,1	1807,5
2500	500	603,9	150,3	1886,8
3000	500	607,4	16,4	1948,3
6000	500	not possible	not possible	-
6000	1000	1336,4	1584,4	2093,6

Figure 2.8: Mode-matching parameters (cavity length  $L$ , focal length of the mode-matching lens  $f$ , calculated distances  $d_1$  and  $d_2$ , cavity waist radius  $W_0$ ). “not possible” refers to non-real results.

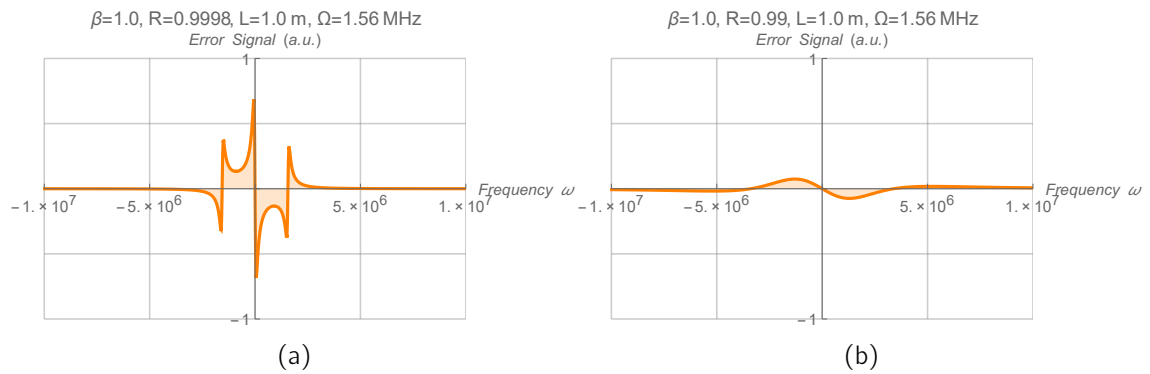


Figure 2.9: Influence of cavity parameters on the PDH error signal (arbitrary units) around the resonance frequency for a modulation depth  $\beta = 1$ . (a) standard values as realized in the experiments (b) in comparison with a lower mirror reflectivity of 0.99

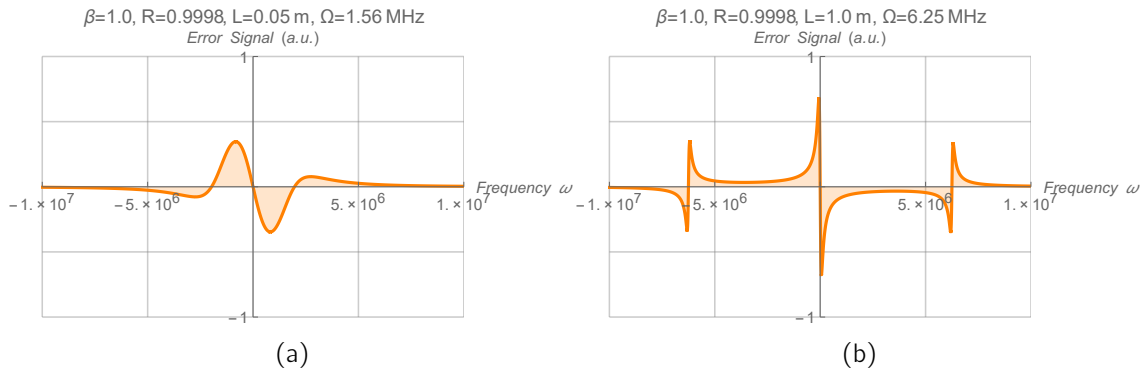


Figure 2.10: Influence of cavity parameters on the PDH error signal (arbitrary units) around the resonance frequency for a modulation depth  $\beta = 1$ . (a) cavity length 5 cm (b) modulation frequency 6.25 MHz

around resonance, in the case of low mirror reflectivity or small cavity length. As expected, the sidebands move out from the center of resonance for higher modulation frequencies (figure 2.10 (b)).

## 2.5 Electrical Noise

A compact overview about noise and some of the appropriate countermeasures follows. As this is more of a practical kind of nature, and owed to the fact that the requirement of noise investigation emerged lately during the course of this work, it is included in the experimental part here.

When measuring small and constant electric signals one will soon discover the fact that there are no absolutely smooth and constant, but instead fluctuating signals. There exist several kinds of noise and a rather simple definition of noise in electric systems could be the following:

“Noise is any electrical signal present in a circuit other than the desired signal.” ([23], p.3)

This is of course somewhat generalizing, and basically one has to distinguish between inherent electronic noise, in the form of random fluctuations, that occurs in e.g. resistors or semiconductors, and noise that is introduced from the outside into a system via some coupling path. Minimizing the first is up to low-noise design of electronic parts and systems; the latter can be degraded by grounding and shielding single electronic components, sections or the whole system. In general a typical noise problem

consists of some noise source, a coupling path and a receptor (compare [23], p. 30). This motivates that several possibilities exist to reduce the noise at the receptor, i.e. a sensitive electronic circuit that has to be protected: after tracking down the noise source, which can be difficult, noise can be eliminated by a replacement of its source or diminished by some shielding. If the coupling path can be influenced, then this would be another possibility to reduce adverse electromagnetic interferences. Finally, one can shield the receptor. However, it is the most effective strategy to eliminate the emission of noise directly at the source. Prominent noise sources, especially in a laboratory environment that electronic systems could be exposed to are e.g. motors, switches, personal computers, switching-mode power supplies, and digital circuits with low signal-rise/fall times (i.e. fast switching speeds).

The existing literature on noise, its reduction and electromagnetic compatibility, opens a wide and complex field that is worth a closer look for any engineer, but for the sake of compactness the author wants to reduce this here to a bare minimum. The reader should keep in mind though, that the information presented in the following is strongly simplifying and incomplete. This applies especially to the theory of grounding and shielding of electrical systems.

## 2.5.1 Inherent Electronic Noise

**Thermal Noise** It is also called Johnson-Nyquist noise and an inherent property of every electrical system. Its origin can be explained with quantum mechanics: when the carriers of electrical charge propagate through a conductor (or resistor), they are randomly scattered at the atoms of the bulk material. This leads to a random time-varying signal which is zero on average. The thermal noise power depends linearly on temperature and is given by equation (2.4).

$$P = 4kT\Delta f, \quad (2.4)$$

where  $k$  is the Boltzmann constant ( $1.38 \cdot 10^{-23}$  J/K),  $T$  the absolute temperature (K) and  $\Delta f$  the bandwidth (Hz) of the system. Equation (2.4) can be written in terms of voltage, which leads to  $U = \sqrt{4kT\Delta fR}$ . This gives rise to the following considerations in order to limit thermal noise: First, cooling or at least temperature stabilization of a system, and second, taking care to separate the signal of interest from frequency components that do not contribute to the measurement, but would

introduce additional noise. Electronic filters can be applied to shape a signal in its frequency domain; e.g. by using a band-pass or a low-pass filter. The distribution of thermal noise power is uniform in frequency space for which the well known term of “white noise” exists. In practice this means that the integrated noise power within a certain frequency interval only depends on the width of that interval and not where it is located in frequency space.

**Other Types of Noise** *Shot noise* is of “white” characteristic and an inherent property of all conductors that occurs when charge carriers flow over a potential barrier; it arises from the particle nature of the charge carriers and their random motions e.g. the recombination of electrons and holes in semiconductors. It can be quantified by (see [23], p. 338)

$$I_{\text{shot}} = \sqrt{2eI_{\text{DC}}\Delta f},$$

where  $e$  is the electron charge,  $I_{\text{DC}}$  the DC current and  $\Delta f$  the bandwidth. It shows that besides bandwidth, shot noise depends on the amount of DC current that flows through a conductor.

*Contact noise* on the other hand, shows a  $1/f$  characteristic (“pink”) and is caused by imperfect electrical contact of two conductors. This leads to a fluctuation of voltage due to the not well defined resistance of the contact that is traversed by a current. It can be problematic at low frequencies (LF) or at DC due to its  $1/f$  characteristic.

This contact noise might be indeed a severe problem, if one considers sub-optimal soldering joints or the aging of cables and BNC connectors.

**Adding up Noise Sources** When more than one uncorrelated noise sources are present in a system one has to sum up the square of all contributing noise voltages, because it is the power that is physically relevant:

$$U_N = \sqrt{\sum_i U_i^2}.$$



## 2.5.2 Grounding and Shielding for Noise-Improvement

**Grounding** One basically has to distinguish between earth ground and signal ground. While the first is an action electricians set for providing safety to humans and living things that are in contact with electric systems, the only meaning of the latter is that of a return path or common connection for signals and currents. For consideration: every electric circuit has to be a closed loop but the functionality of a circuit depends not on whether there is an *earth* ground connection or not. In some cases the noise of a system might be adversely influenced if it is connected to earth ground, as one can see from the following: the earth ground system consist of long cables which act as receiving antennas. It is therefore receptive for any kinds of noise through capacitive and inductive coupling. In addition, the earth ground may be loaded with noise currents from other electrical equipment. Therefore, in most cases, one should avoid an earth ground connection, from a noise reduction point of view, which is not always possible as one has to meet the safety regulations first. There exist several grounding schemes that can be applied depending on the circumstances of a system. For low frequencies (DC to 20 kHz) a single point ground can be used (see [23], p. 124). Here all return paths are connected in one and only one point, whereby these connections can be made either in series or in parallel. If the connections are in series (“daisy chain”), this leads to the following problematic situation: consider a system of several points that shall be grounded; due to only one common return path for all grounding points, the different path-lengths of the conductors introduce a different impedance back to ground for each of the grounding points. If a certain, respective current flows back out of each grounding point, the potential drop over the different impedances leads to a cross coupling of the potentials between the grounding points. The voltage drop over the impedance of one conductor section within the daisy chain influences the grounding potentials of all the following elements. In other words: a current that flows out of one grounding point directly influences the grounding potential of the adjacent grounding point and so on. If this current is time-dependent with some frequency  $\omega$ , then the other grounding potentials that are connected will oscillate at that same frequency. This can be avoided by a parallel configuration of return-conductors, ending in the same single point. However, due to the large inductance of ground-conductors, the single point grounding scheme does not work at high frequencies (HF). A HF-current is suppressed by the increasing inductance (consider the inductive reactance  $X_L = \omega L$ ) of a wire. But since currents flow in closed loops, another path opens that offers a low reactance (consider the capacitive

reactance  $X_C = 1/(\omega C)$  ) at HF: capacitive coupling through the omnipresent stray capacitance to ground, which effectively leads to a multi-point ground. Therefore at higher frequencies a common ground-plane makes sense.

**Shielding** Since James Clerk Maxwell postulated his famous equations in the 19<sup>th</sup> century everything about electrostatics, magnetostatics and electrodynamics is known. For instance, a charge carrier is the source of a static electric field. If a charge carrier moves a magnetic field is generated in form of a closed loop. An oscillating dipole radiates electromagnetic waves out into the space. Different field sources that could introduce noise have to be treated differently, as one can see from the following: a static electric field is easily shielded by a Faraday-cage i.e. an electrically conducting enclosure. The electric field influences the free charge carriers of the conductor to build up a field that exactly cancels the outer electric field, leading to a field-free inner space of the enclosure (i.e. the shield). And this can be inverted: a charge within a conducting enclosure will lead to no electric field at the outside of the shield. Static magnetic fields, on the other hand, are hard to shield. One has to use materials with high permeability like mu-metal to confine the magnetic field lines (compare [23], p. 204). If the magnetic field is quasi-static, i.e. a slowly varying field, then one essentially observes, according to Faraday's law of induction, the emergence of eddy-currents. These eddy-currents increase with frequency and electric conductivity of the shield, and produce a magnetic field that compensates the outer magnetic field. This effect becomes more and more effective at higher frequency, explaining the functionality of an electromagnetic shield (compare [24], p. 101-102). One should add that the impact of a magnetic field is most effectively reduced by minimizing the area of the interaction loop, which is given by the total area that is enclosed by a current of a circuit (compare [23], p. 67). This is of course again a consequence of Faraday's law of induction<sup>5</sup>.

**Cable Shielding** A cable that is unshielded or improperly shielded works as an efficient receiving and emitting antenna, and it is therefore of great importance to pay attention that shielded cables are used correctly. This involves the selection of the appropriate cabling, as well as the proper shield termination, i.e. if - and at what point - a shield has to be grounded or not. If one takes a look at a coaxial cable, it is obvious that the outer shield provides two functions: first it works as a shield,

---

<sup>5</sup>As of reference ([16], p. 125) this is  $U_{\text{ind}} = -\frac{d}{dt} \int \vec{B} \cdot d\vec{A}$ , with  $\vec{B}$  the magnetic field, and  $d\vec{A}$  the infinitesimal surface vector element

and second as a return path for signals. If a magnetic field emitted from some other conductor (i.e. a noise source) induces a current into the shield, it is important to ground the shield at both ends in order to conduct the currents that are induced into the shield to ground. However, one can show (compare [23], p. 56) that the currents in the shield induce a current in the center conductor due to the mutual inductance between the shield and the center conductor. These currents cannot be suppressed by any non-magnetic shield, and there exists a low-cutoff frequency for any certain shield-configuration that is proportional to the shield resistance<sup>6</sup> ([23], p. 60, equation 2-26). In the case of the all too common RG-58 coaxial cable this limit<sup>7</sup> is at around 2 kHz (see [23], p. 62, table 2-1), providing that slowly varying magnetic fields cannot be shielded, even if the shield is grounded at both ends ([23], p. 62). If the magnetically induced shield currents are prevented from flowing in the shield by not grounding the shield or grounding it only at one end, the magnetic field shielding is useless above the low-cutoff frequency (compare [23], p. 64, figure 2-17), and the center conductor is completely unshielded against magnetic fields. To summarize that: low impedance grounding of a coaxial cable at both ends provides good magnetic shielding above the low-cutoff frequency, but there is no way to shield against static or LF magnetic fields below the low-cutoff frequency by use of conductive non-magnetic shielding materials. To circumvent the lack of a coaxial cable shielding against LF magnetic fields, one can use shielded twisted pairs instead (compare [23], p. 88) because the twisted conductors protect against the coupling of magnetic fields by their mutual inductance.

In the LF domain one usually terminates the shield of a coaxial cable on one end (compare [23], p. 89). This eliminates the coupling of e.g. power-line noise (50/60 Hz) and possible ground-loops. However, in this case there is no shielding against HF magnetic fields, and therefore the cable becomes an emitting and receiving antenna. Additionally, if the shield that is terminated at one side of a housing is connected to a circuit's common, this HF-noise is coupled into the circuit. Therefore, one should avoid making this connection, and instead terminate the cable shield at the enclosure

---

<sup>6</sup>Therefore a low shield resistance is of great importance, and one should bear in mind that this resistance is the sum of all conductors that are connected to a grounded shield. Essentially this means that the best conducting shield is useless against magnetic field shielding if it is terminated with a high resistance

<sup>7</sup>Actually things are worse: one has to take approximately 5 times the cut-off frequency because this would sufficiently exceed the 3 dB corner frequency. This means a 10 kHz low-cutoff frequency for a RG-58 coaxial cable (see [23], p. 62, table 2-1)

by the lowest impedance path possible (compare [23], p. 89).

For noise improvement in the HF-domain the shield connection is much more important than grounding. If the connection between two shielded housings is made up by a shielded cable, the shield of the cable ideally should extend the shield of the enclosure. To sustain the integrity of the whole shield, the cable shield has to be connected on both ends of the cable, and additionally, have a good electrical contact on 360° around the cable. Pigtail connections<sup>8</sup> have to be avoided (compare [24], p. 383).

An interesting option in grounding a cable shield is offered when using a triaxial cable. Its design provides two independent coaxial shields around the center conductor. The outer shield can then be connected to the conducting enclosures, providing an extension of their shields, and therefore an effective shielding against HF-fields. The inner coaxial shield can be used as a signal ground that is protected from external HF-field coupling by the outer shield.

Finally, it shall be mentioned that one should also pay attention to the fact that the lifetime of a cable with a braided shield will shorten if it is frequently moved. The friction between the single filaments produces additional abrasion, which can approximately shorten the lifetime down to a third. One of the most common sources of failure, even of professional tailor-made cables with a braided shield, is the connection between the shield and the HF-connector. This connection is subject to strong aging when stressed with frequent movement, and adversely alters the vitality of the HF-shield (see [24], p. 371).

**Grounding of a Shield Enclosure** A shield that is completely closed, forming a Faraday-cage, does not have to be grounded to be effective<sup>9</sup>. However, the shield should be connected to the circuit common in order to prevent any differing potentials between the circuit and the surrounding shield (compare [23], p. 296). In addition, the earth-grounding of a shield effectively conducts away static electric charge that would otherwise cumulate on the shield.

---

<sup>8</sup>Connection of the entire cable shield in only one point to the shield of the housing, and not around the entire cable shield

<sup>9</sup>As mentioned above this still does not provide any protection against static or LF magnetic fields

**Filtering of HF-Noise using Ferrites** Ferrites represent a practical and efficient low-cost measure and introduce a large HF-impedance in a circuit, without producing a noteworthy resistance at LF or DC (compare [23], p. 225). These filters are easily attached on the outside of a wire or a coaxial-cable (snap on), and can provide significant HF-noise filtering from around 1 MHz up in the GHz range (compare [23] p. 226-227). One should note, that the use of multiple turns of a wire around a ferrite core ring is a common practice, leading to an increase of the inductive reactance. But one should consider that this also increases the capacitance between the windings, and therefore degrades the HF capacitive reactance (compare [23], p. 228) and leads to a lower filtering efficiency at higher frequencies. In conclusion, one should use several windings around a ferrite core if HF in the lower domain have to be filtered, and up to one winding if the filter has to be effective in the HF-domain. Furthermore, there exist several ferrite materials from different manufacturers, all of them showing different impedance behavior as a function of frequency, which results in a variety of HF-filtering performance. But one rule applies to all and shall not be overseen: the longer a ferrite core, the larger its impedance, and the higher its filtering capabilities. Moreover, ferrite cores not only act effective in reduction of conducted noise but also in reducing the radiated emission (antenna) of a cable (compare [23], p. 233).

## 2.6 System Noise Investigations and Countermeasures

At the beginning of the experimental part of this work the author was not aware of the strong impact electronic noise can have on a laser output signal. This noise can be understood as some unintended modulation that is applied on the laser emission. Several noise sources were discovered in the setup and lab and consequently eliminated, or in some case diminished by grounding and shielding-measures by using the methods described above. For example, fully enclosed aluminum metal boxes served as effective HF-shields for the protection of some electronic circuitry. For the standard connections shielded RG-58 or RG-174 coaxial cables with BNC, SMA or SMB connectors were used. The whole system was built up on an optical bench, made from massive steel. It served as a reasonable common ground plane as suggested above, and should have provided a good capacitive coupling return path for noise signals in the HF-domain. For safety reasons, the bench was connected to a recently new installed lab earth ground of 26 mm cable diameter. A single point ground on top

of the bench, where all ground connections of the components were linked together on a polished copper plate, was established. The copper plate ( $10 \times 10$  cm) had a direct low impedance contact to the optical table. The earth ground was connected to its center. This approach should offer both, HF-grounding by the common ground plane, and LF-grounding by the single point ground connections.

A spectrum analyzer<sup>10</sup> came in as very useful tool for investigating the frequency domain of signals, and for tracking down noise sources. An oscilloscope displays electric signals in the time-domain. Triggering selects a wave of the possibly extensive noise spectrum. In comparison, a spectrum analyzer opens the view to the frequency domain, and is capable of logarithmic visualization of the signal amplitudes, therefore acquiring a larger dynamic range of signals. It provides simultaneous view of noise-peaks located at different frequencies, detected in one frequency-sweep. A typical measurement of the signal noise floor of the utilized photo-detector (Vigo) was approximately -110 dBm at a resolution bandwidth of 1 kHz, whereas the smallest voltage-scale adjustable on a common digital oscilloscope is in the 1 mV/div region<sup>11</sup>, which makes e.g. a 3 dBm peak, occurring at a noise-floor of that size of order invisible on an oscilloscope.

To overcome problems with different potentials between devices and grounding points, and moreover, to improve the shielding, triaxial-cables were utilized for connecting the laser-driver to the QCL. As mentioned in the preceding, in contrast to conventional BNC-cables (as RG-58 or RG-174) triaxial-cables (e.g. Belden 9222) feature an additional outer coaxial shield around the inner coaxial shield and the innermost core wire. The literature suggests two reasons for using a double-shielded cable ([23], p. 93): first to increase the HF shielding effectiveness, and second, if low and high frequency signals are transmitted over one and the same cable. This applies to the current work, since the connection from the laser driver current output to the QCL input carries a basic DC signal for the operation of the QCL, a slow scan signal, which is of triangular waveform up to 100 Hz in frequency<sup>12</sup>, and additionally the faster modulation signal with a frequency of at least 1.56 MHz to generate the sidebands utilized in the PDH-technique.

---

<sup>10</sup>Agilent 4395A, 0-500 MHz

<sup>11</sup>For comparison: at  $50 \Omega$  termination e.g. -100 dBm equals  $2,236 \mu V_{\text{rms}}$ , -40 dBm equals  $2,236 \text{ mV}_{\text{rms}}$

<sup>12</sup>A frequency domain measurement showed Fourier-components up to approximately 5 kHz

The connections between the TEC-housing and the QCL protection-circuit housing were equipped with triaxial panel-mount connectors. In more detail, the TEC-current connection, the NTC-sensor connection and the QCL current-input connection were equipped with triaxial panel-mount connectors. The appropriate triaxial-cables were tailor-made in house. As there were no triaxial panel-mount connectors with isolated outer shield commercially available, the first approach was to craft the triaxial-cable in a way that the outer shield was not connected; it has been isolated by PTFE foil within the cable between the shield and the outer shield cable clamp. While at a first glance this might be useful to isolate ground loops by avoiding direct electrical contact (which was approved by a check of the shield conductivity) a more practical view reveals a problem with this: any isolation of two conductors by an insulating material introduces a certain amount of capacitance to the signal path; while this might be useful in the LF domain, working as a break up for the circuit to avoid ground-loops and different potentials, it might be a short circuit in the HF domain due to the low impedance at high frequencies; this may lead to adverse noise effects in the HF-domain, and sometimes to more noise than caused by ground-loops and potential differences.

A solution to this dilemma can only be determined by trial and error, and consequently going then for the lower noise approach. As Henry W. Ott writes in his book about electromagnetic compatibility engineering, there is not only one solution to solving a grounding problem, and two different engineers might come to different solutions to a certain problem (compare [23], p. 123):

“Another factor to keep in mind is that grounding always involves compromise. All ground systems have advantages as well as disadvantages. ...grounding problems have more than one acceptable solution. Therefore, although two different engineers often will come up with two different solutions to the same grounding problem, both solutions may be acceptable.” ([23], p. 123)

A wider view in this context emphasizes that a certain noise problem might never be entirely eliminated but instead a satisfying solution can be found, and, moreover, this procedure is not always straight-forward.

Consequently the following approach was carried out: the outer shield of the triaxial cables was electrically connected on both ends to the panel-mount triaxial-connectors

outer shield; the inner shield served as a return path for the signals and was therefore isolated from the involved enclosures.

The process of noise investigation and improvement was iterative, as shall be shown by the following example: after eliminating the noise that was emitted from the temperature controller, which was equipped with switching elements (most likely based on pulse width modulation) and coils, by substituting it with a linear temperature controller, the connection from the control electronics (Digilock) to the modulation input of the laser-driver was investigated. Excessive noise showed up with a major peak at 100 MHz (peak amplitude -65 dBm at a noise floor of -110 dBm (see figure 2.11), most likely coming from a clock-frequency from the internal electronic circuitry of the Digilock device<sup>13</sup>. If one takes a closer view on the spectrum in figure 2.11 it is clear that a very large amount of noise was introduced by this device. A passive  $LC$  pass-band as an intermediate connection in a shielded aluminum case with two BNC-connectors attached, in combination with multiple ferrite core rings mounted on the outside of the coaxial-cables between the Digilock (main out) and the modulation input of the laser-driver, was investigated to be an effective counter-measure against this noise-source.

The connection between the laser-scan output of the Digilock (SC110 out) and the analog input of the laser driver was observed to introduce most of the noise onto the laser signal. First, a passive filter-approach failed, as there were still considerably large peaks left in the frequency spectrum. A second approach used an active  $RC$  low-pass filter, based on an operational amplifier circuit in a shielded aluminum case, built as an intermediate filter with two BNC-connectors attached. It could be investigated that this configuration attenuated the noise in the entire frequency spectrum almost down to the floor (-110 dBm). However, it also had an unwanted effect: the damping of a sinusoidal test signal was too large, and showed that this approach was not practical. Consequently, the active filtering was again replaced, this time with a  $LC$  low-pass filter with a cut-off frequency of 5 kHz. This particular value had to be chosen because of the frequency spectrum of the applied laser scan. The scanning-waveform generated by the Digilock device is of a triangular shape with a typical frequency of approximately 10 Hz. Hence, it contains a Fourier-spectrum of higher order frequency components (harmonics), i.e. multiples of the

---

<sup>13</sup>Indeed, the datasheet revealed a 100 MHz FPGA clock frequency



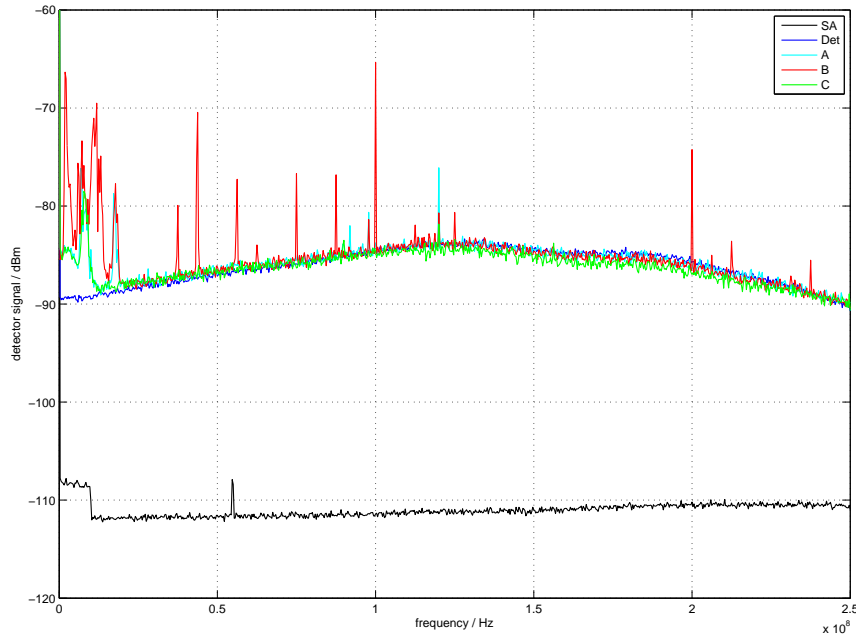


Figure 2.11: Noise power spectrum (dBm) in the range 0-250 Mhz, resolution bandwidth 1 kHz. All measurements with averaged data acquisition (5x). The data plotted in red color indicates the system without any countermeasures, whereas the data plotted in green color shows the improved noise power spectrum after applying specific countermeasures. SA: noise floor of spectrum analyzer, Det: noise floor of detector. For a detailed description of configurations A, B, C refer to the text

10 Hz ground-frequency.

**Laser Signal Noise Measurements** For the purpose of these measurements the optical setup was slightly modified; in fact it was simplified by placing the photo-detector (Vigo) right after the optical isolator in the beam path (see figure 2.2). The laser current was set to 220 mA at a TEC temperature setpoint of around 22°C. The obtained results, i.e. the noise power spectra in dBm, are plotted in figure 2.11, 2.12, 2.13, and 2.14. For the measurement of the spectrum analyzer's noise floor the signal connection was removed from the analyzer input. The noise floor of the photo-detector was measured by covering the detector-element.

**Configuration A** All cables without ferrites attached; triaxial cables from laser to the laser driver, and from the TEC to the laser; no connections between the laser driver and the control electronics unit (Digilock).

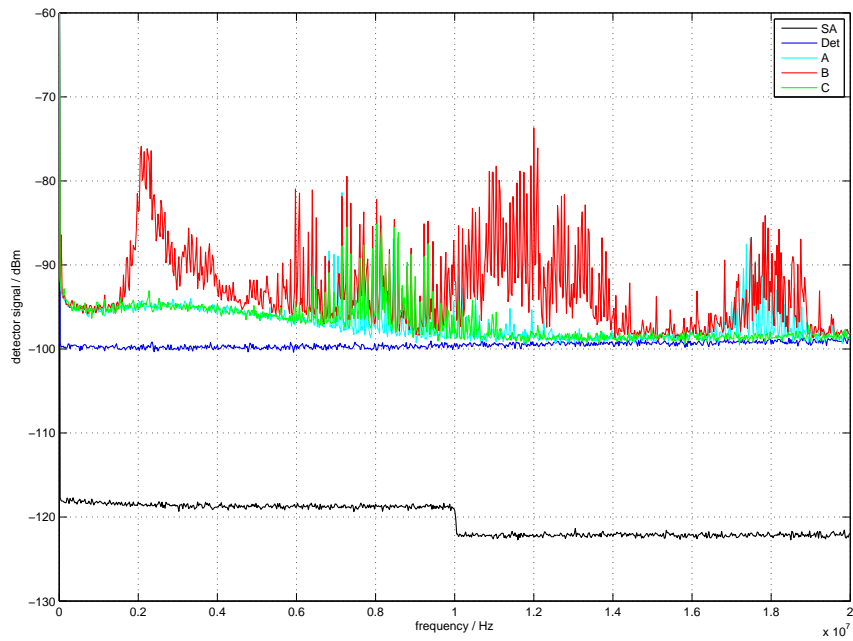


Figure 2.12: Noise power spectrum (dBm) in the range 0-20 MHz, resolution bandwidth 100 Hz. All measurements with averaged data acquisition (5x). The data plotted in red color indicates the system without any countermeasures and turned on PDH-electronics, whereas the data plotted in green color shows the improved noise power spectrum after applying specific countermeasures. SA: noise floor of spectrum analyzer, Det: noise floor of detector. For a detailed description of configurations A, B, C refer to the text

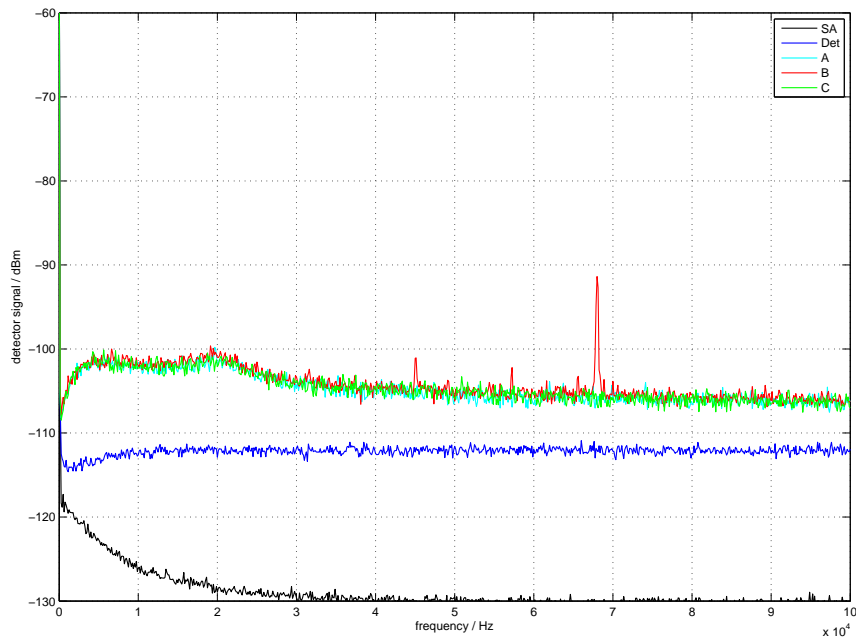


Figure 2.13: Noise power spectrum (dBm) in the range 0-100 kHz, resolution bandwidth 10 Hz. All measurements with averaged data acquisition (5x). The data plotted in red color indicates the system without any countermeasures and turned on PDH-electronics, whereas the data plotted in green color shows the improved noise power spectrum after applying specific countermeasures. SA: noise floor of spectrum analyzer, Det: noise floor of detector. For a detailed description of configurations A, B, C refer to the text

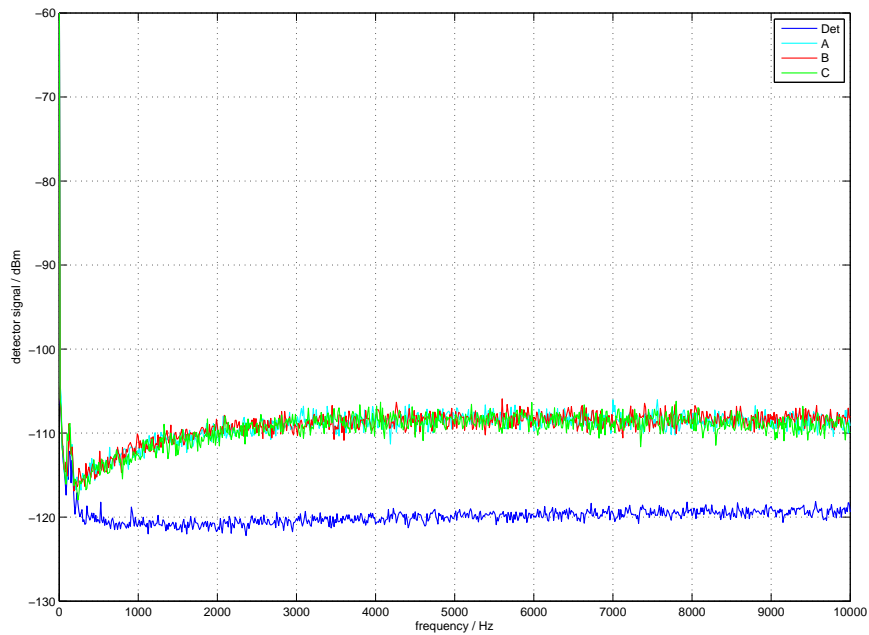


Figure 2.14: Noise power spectrum (dBm) in the range 0-10 kHz, resolution bandwidth 3 Hz. All measurements with averaged data acquisition (5x). Det: noise floor of detector, for configurations A, B, C refer to the text

**Configuration B** Similar as in configuration A, but now with all electrical connections between the Digilock and the laser driver.

**Configuration C** Similar as in configuration B, but now with all countermeasures as described above: *LC* filters on both connections between the Digilock and the laser driver (scan and modulation). Additionally, ferrites were attached on the outside of the cables.

As one can see by comparison of figures 2.11 and 2.12 by means of configuration B and C, the actions that were set, lead to some improvement of noise performance. The averaged noise power (dBm) measured in the system bandwidth 0-20 MHz (801 data-points) at a resolution bandwidth of 100 Hz, relative to the photo-detectors noise floor (Det) is as follows (compare with figure 2.12):

- Configuration A: 2.72 dBm
- Configuration B: 6.57 dBm
- Configuration C: 2.64 dBm

Therefore, the averaged improvement of noise-performance (0-20 MHz bandwidth) between configuration B and C is 3.93 dBm. However, there is still further improvement preferable, especially in the LF domain below 300 Hz. As an anticipation to the last chapter reference [25] motivates that in practice it is the LF noise only that contributes to a broadening of the Lorentzian linewidth of a laser, and therefore it would be highly appreciable to reduce the LF noise in the system. This may be achieved by the use of twisted-pair cables, because, as one has seen above, they provide effective LF magnetic field shielding.

An interesting observation can be made by means of figure 2.12 for all configurations A, B and C: obviously the detected laser signal shows a relatively broad noise spectrum, starting from the very low frequency end, reaching up to around 12 MHz with, on average, a 10 dBm difference with respect to the detectors noise floor. At the time of writing the author is not able to give an appropriate explanation of its origin, but it seems that all of the applied measures have no influence on this.

## 2.7 Experimental Approaches

Different approaches have been carried out during the course of this work. As it is not the author's intention to pretend anything in advance, the reader shall now be enlightened about the fact that measurements based on the following approaches did not lead to the intra-cavity build-up targeted at the beginning of this work, nor any frequency stabilization as was the initial aim. As will be discussed in the final chapter this might have several reasons. With this along comes the fact that there are no actual measurement data, nor any analysis that can be present here, which is truly not satisfying.

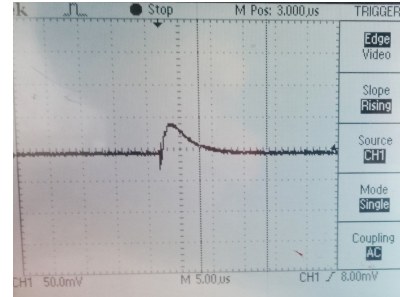
Early approaches were based on a cavity with a length of 5 cm and the custom-made laser driver. The laser scanning frequency was set to 0.1-10 Hz with a triangular waveform, and the amplitude of the scan was set to cover at least one free spectral range. A modulation frequency of 12.56 MHz was applied with an amplitude at the laser output of lower than 1 mA. The high speed photo-detector (Vigo) was positioned to pick up the reflected signal. This setup was also tried with 10 cm cavity length and about 5 mm (as close as the mirror mounts allowed). In all of these approaches nothing like an error signal was visible. Different phase angles were

tried out to compensate for phase delays between the local oscillator of the modulation signal and the detector signal. As the reflected signal still did not show any evidence for intra-cavity resonance, the transmission signal was investigated with a liquid nitrogen cooled MCT-detector (Infrared Associates). For this purpose, the MCT detector was positioned right behind the output mirror of the cavity, and the signal was monitored with an oscilloscope. From time to time there was some sort of a signal visible that was not repeatable on a regularly basis though. It was therefore classified as noise or any kind of a random event.

After the recognition of electronic noise within the laboratory, it was assumed to have adverse influence on the build-up of resonance. So the focus was set on the iterative process of noise investigation and reduction by using grounding, shielding, filtering measures, supported by monitoring of the attained effects with the spectrum analyzer. Then another approach was carried out with an independent battery power supply, linear TECs, grounding measures, shieldings and housings, which again lead to no measurable cavity resonance. Nevertheless, the overall noise performance of the system was improved. As the development of the custom-made laser driver stopped, a commercial laser driver was utilized leaving the same results behind. Finally, the whole system was isolated from air flows, as they were suspected to cause additional noise and interferences on the laser signal, by a local change of the refractive index of air with temperature and pressure fluctuations. A full enclosure from the laser source along the whole beam-path was built up, and the resonator length was set to 1 m. Increasing the frequency sweep speed as suggested by reference [26] produced no measurable and repeatable transmission signal either. The frequency sweep speeds applied were limited by the specifications of the Digilock device and covered 0.1-10 kHz.

**Addendum** In the very end of this work it was possible to see decaying signals that were quite similar to typical cavity ring-down signals (compare with [17], p. 36) showing exponential decay (see figure to the right), and therefore motivating the emergence of a small partial build-up of intra-cavity resonance. The resonator length was chosen to be 1 m and the system was completely isolated by some enclosure to suppress air flows and acoustic noise. The LN<sub>2</sub>-cooled MCT detector was placed behind the cavity output to measure any transmission. The oscilloscope was set to single-shot trigger mode to monitor

any cavity output. From time to time, a fast rising but weak signal was visible, showing exponential decay with a time constant in the approximate order of the cavity's



ring-down time of 16.7  $\mu$ s. And these signals did not occur if the laser was switched off. This is a promising result and deserves further investigations.

# Chapter 3

## Results and Discussion

After several approaches with different cavity lengths and optimizations during a long run in the lab to achieve ongoing and stable resonant conditions within the optical resonator, eventually all of them failed. The wide-spread literature that exists on resonant optical cavities motivates that it is straight-forward to excite cavity modes by use of a laser source to achieve resonant conditions. A proper mode-matching calculation was carried out, and the according measures were accomplished on the bench. To the best of the author's knowledge the laser beam alignment was done precisely and with care. As a central aspect of this work the entire laser-system was improved in its noise performance by building up a completely independent battery power supply; by grounding and shielding as well as electronic signal-filtering, which in sum lead to a significant improvement of noise (refer to figure [2.12](#)). Finally, it was possible to see a decaying signal that provided some indication of a partial intra-cavity intensity build-up. However, on a repeatable basis it was not possible to measure cavity signals in reflection or transmission that would have indicated a significant intensity build-up within the resonator. Besides the probable presence of an additional hidden systemic error, one thing that is undoubtedly of great importance is probably clarified with the following quotation:

“Intrinsic phase noise is responsible for the finite laser Lorentzian width or equivalently for its finite coherence time and actually prevents achievement of a steady state of the field injected into the cavity when the laser linewidth is close to or larger than the cavity resonances.” [\[26\]](#)

This gives rise to the following considerations: the linewidth of the used QCL source is broadened due to the intrinsic noise of the current driver, and dominating other random phase and especially LF noise sources that are still present in the system.



The linewidth of the utilized high-finesse cavity is approximately in the range of several kHz, while that of the free running QCL is with no doubt in the MHz-range (e.g. see [11]). Since the laser linewidth is inversely proportional to the coherence time (i.e.  $\Delta\nu \cdot \tau_{\text{coh}} = \text{const}$ , see [18], p. 177), the phase fluctuations of the laser are critical if they are on an equivalent timescale or even faster as the cavity build-up time. This fluctuating phase effectively prevents the intensity build-up due to the deficiency of constructive interference within the resonator.

The allegation above is confirmed in [26] that in the ideal case two things are needed to get a good cavity-performance: one is that the coherence time of the laser should be much longer than the response time of the cavity (which is equivalent to a laser linewidth that is much narrower than the cavity mode linewidth). The second is that the frequency scan should be adiabatic<sup>1</sup>, i.e. the time for one complete scan through a cavity mode should be long in comparison to the response time of the cavity. Their conclusion [26] is that for the use of a high-finesse cavity, with a typical mode bandwidth of several kHz, it is required to have an ultra-narrow laser source. This is supported by [27], where a laser source with a free running linewidth of 5 kHz was employed in combination with a high-finesse vacuum mounted cavity that had a finesse of 18000 and a linewidth of 10 kHz.

For comparison, another practical example is shown by means of a well-known technique called ICOS (Integrated Cavity Output Spectroscopy): in a typical ICOS setup the finesse is commonly chosen to be about  $10^4$ , with a cavity mode linewidth of about 10-100 kHz and a laser linewidth of typically less than 100 kHz [26]. And, to point out, this technique is reported to be known of being more tolerant to variations in laser linewidth and frequency scanning speed [26].

The Pound-Drever-Hall technique is capable of dealing with such phase (or frequency) noise of a laser source as stated in [20]. Even if the laser linewidth is broader than the cavity mode linewidth the technique succeeds, because the sidebands that are directly modulated on the carrier always have a fixed phase relationship relative to the fluctuating phase of the carrier. But what if the stable reference of this technique, i.e. the optical resonator, shows instabilities? The phase information in the sidebands is measured with respect to the cavity's resonance frequency. This motivates

---

<sup>1</sup>This was ensured in the experiments by a maximum scan frequency in the range of 10-100 Hz, i.e. at least a time duration of 10 ms for one frequency scan versus  $\tau_p \approx 16.7 \mu\text{s}$  response time of the cavity, which is a ratio of about 600

that the employed PDH-setup is probably not capable of starting up a functioning feedback-loop, in order to actively narrow the linewidth of the laser because, due to mechanical instabilities, the center of a cavity mode is not fixated enough in frequency space, causing some dithering of the resonance frequency. To see that, consider the following simple calculation: if one takes the resonance frequency of an optical resonator  $\nu_n$  which is

$$\nu_n = n \frac{c}{2L}, \quad n = 1, 2, \dots$$

and differentiates by the resonator length  $L$ , one obtains after rearrangement

$$d\nu_n = -n \frac{c}{2L^2} dL = -\nu_n \frac{dL}{L},$$

which shows that the relative change of resonance frequency is given by

$$\frac{d\nu_n}{\nu_n} = -\frac{dL}{L}. \quad (3.1)$$

If one puts in the numbers according to the experiment (center wavelength  $\lambda = 4.59 \mu\text{m}$ , cavity mode linewidth  $\Delta\nu = 9543 \text{ Hz}$ , resonator length  $L = 1 \text{ m}$ ), one has:

$$\frac{9543 \text{ Hz}}{6.53 \cdot 10^{13} \text{ Hz}} = -\frac{dL}{1 \text{ m}}.$$

It follows that a length stability of

$$|dL| = 1.46 \cdot 10^{-10} \text{ m}$$

would be appreciable, which is in the order of atomic length scales. Therefore, a good mechanic stability of the resonator could be advantageous to minimize cavity noise. Even if one allows for a cavity mode a linewidth of 1 MHz, which could only be realized with a lower finesse, one would still need a length stability of  $|dL| = 1.53 \cdot 10^{-8} \text{ m}$ . And this discussion could also be extended concerning fluctuations of temperature and refractive index<sup>2</sup> of the cavity medium. The modulation frequencies applied in the experiments reached from 1.56 MHz to 6.25 MHz<sup>3</sup>, which probably is too small in comparison to the fluctuations of the cavity resonance frequency, leading to sidebands that do not carry the phase information relative to a stable reference as

---

<sup>2</sup>Which depends on temperature and pressure

<sup>3</sup>The modulation bandwidth is limited by the specifications of the laser driver (QCL 1000), although the control electronics is capable of providing a modulation frequency up to 25 MHz

expected. If one considers the narrow linewidth of a cavity transmission in combination with the dithering of its central frequency (i.e. the resonance frequency) due to vibrations, the following problem arises: while this might not be too problematic for a broader linewidth, i.e. a cavity with lower finesse, and therefore more uncertainty regarding the transmission linewidth, it is far more problematic for a narrow linewidth if one compares the linewidth relative to the resonance frequency deviation. In conclusion, the deviation of the resonance frequency should be not more than at least equal to the cavity mode linewidth. To give an example: if one assumes a reasonable mirror-position uncertainty of 1 nm, one can translate this by use of (3.1) into an uncertainty of the resonance frequency of about 65 kHz; if one compares this to the cavity linewidth of 9543 Hz, one notes that the ratio of the position uncertainty of the central peak to its width is about 7, and would therefore have significant influence on the build-up of intra-cavity field. So far the time scales on which these vibrations could have significant influence have not been considered, as this will be done further down.

Consequently, if there is no resonance achievable at any time during a laser frequency scan, covering more than one free spectral range, then there is no point for the PDH feedback-loop to start with and the technique fails.

In conclusion, the mis-achievement of stable resonance within the resonator is a not only a consequence of the initially broad linewidth of the laser, but more a combination of this with the additionally not well defined resonator frequency, and moreover, the high finesse of the resonator. The finesse is crucial because, due to the extremely narrow linewidth of the cavity mode, high precision is demanded in all technical belongings. A solution to all of this is most likely a combination of the following measures: a cavity with more mechanical stability against acoustic vibrations and pressure changes should be considered. On longer timescales, which is less critical for intensity build-up but important for a stable reference, even thermal stability of the cavity could improve the passive resonator stability; this could be achieved by a temperature stabilized vacuum chamber with a fixed mirror distance and with glued mirrors; additionally one could make use of materials with a low thermal expansion coefficient like Invar or Zerodur to have lower dependency on thermal expansion that would lead to some cavity resonance drift on longer timescales. An example for optical stabilization of a QCL where Zerodur was used is given in reference [28]. The use of a lower noise current driver in a lower noise environment or even more sophis-

ticated shielding and filtering measures could be applied. Shielded twisted pair cables could be used for all signal connections to suppress LF inductive coupling of magnetic fields. In addition, housings could be shielded against LF magnetic fields by use of materials with high permeability like mu-metal. Furthermore, it would be interesting to determine the natural linewidth of the employed QCL by some additional experiment. In the case of finding an exceptionally broadened natural linewidth a lower noise QCL source could then be considered. Tombez et al. have shown [30], that there could be a significant difference in noise performance between two buried heterostructure 4.55  $\mu\text{m}$  DFB-QCLs out from the same production run. They proposed that the different noise performance arose from a difference in thermal resistance of the two devices. Moreover, active linewidth narrowing of a mid-IR QCL has been recently shown, which is based on a purely electrical feedback control without any optical reference [29]. It would have to be evaluated if the PDH-technique could be combined with such a pre-stabilized QCL. Alternatively, one could make use of a system with a lower finesse, i.e. mirrors with a lower reflectivity, if this can be tolerated within the scope of a certain future application.

To be a bit more specific and to substantiate the speculations regarding the current driver presented above, one should take a view on the fact that the commercially available low-noise laser current driver used in this work has a spectral current noise density of  $2 \text{ nA}/\sqrt{\text{Hz}}$ . If one takes into account the minimal PDH modulation bandwidth of 1.56 MHz that was fed into the driver, one ends at least up with a RMS current noise of  $2 \text{ nA}/\sqrt{\text{Hz}} \times \sqrt{1.56 \cdot 10^6 \text{ Hz}} \approx 2.5 \mu\text{A}_{\text{RMS}}$  or expressed in peak to peak  $2\sqrt{2} \times 2.5 \mu\text{A}_{\text{RMS}} \approx 7.1 \mu\text{A}_{\text{p-p}}$ . This is the minimal current noise of the whole system - or rephrased - as good as it can get. We have seen in section 1.1.1 that the main contribution to the noise performance of a QCL in most cases is given by the current driver, and not dominated by the natural linewidth of the QCL. Any additional noise sources (that are undoubtedly present in the system) or a higher system bandwidth would increase this value even further. The cavity mode linewidth for a finesse of  $\mathcal{F} \approx 15706$  and a cavity length of  $L = 1 \text{ m}$  is  $\Delta\nu \approx 9543 \text{ Hz}$ , which can be transformed into a laser current range by the use of the current tuning factor of the QCL ( $-0.6 \text{ cm}^{-1}/40 \text{ mA}$ ), and determined to be  $I(\Delta\nu) \approx 21 \text{ nA}$ . The corresponding FSR expressed in terms of a current would be  $I(\nu_{\text{FSR}}) \approx 333.3 \mu\text{A}^4$ . Consequently, in terms of a current, the RMS-linewidth of the laser is approximately

---

<sup>4</sup>Of course these two quantities are related by the finesse:  $\mathcal{F} = I(\nu_{\text{FSR}})/I(\Delta\nu)$

120 times larger than the cavity mode FWHM linewidth, making the build-up of resonance very unlikely. Furthermore, the build-up time for a lossless cavity<sup>5</sup> of that length and finesse is  $\tau_p \approx 16.7 \mu s$ . This means, according to  $\Delta\nu \cdot \tau_{coh} = \text{const} = C$  (with  $C = 1$  for simplicity as of [18], p. 177), one demands a linewidth of the laser of at least 60 kHz to be coherent enough for a complete intensity build-up. In turn, if one assumes a generic DFB-QCL linewidth of around 10 MHz (which is very likely the case for the used QCL) this would mean a laser coherence time of  $0.63 \mu s$ , which shows that the build-up time of the utilized cavity is more than 26 times larger than the coherence time of the QCL, preventing a full intra-cavity intensity build-up. One should add that even a slow scanning of the laser frequency, covering more than one FSR of the resonator, and without applying any signal modulation, can not and did not overcome this linewidth discrepancy.

From one of the experimental approaches it turned out that it was even impossible to produce any transmission signal if the laser driver was completely isolated from any input signal that could introduce a certain noise bandwidth. In this case the system noise was the lowest possible to be reached with this setup. The cavity's resonance-wavelength tuning was achieved by hand with a precise change of the cavity length with the adjustable micrometer stages. The conclusion of this experiment, which is of course in terms of the realized version of the PDH-technique in this work<sup>6</sup> a somewhat unpractical approach, could be that even if the driver noise can be diminished by eliminating all input signals, there still is some noise present in the system. May it be the noise of the unstable cavity itself or the noise that is inherent to the laser. Something in the system is leading to a linewidth broadening, which equivalently leads to an insufficient coherence time of the laser. This effectively prevents the resonant build-up of an intra-cavity field amplitude.

**Further Discussion regarding Cavity-Resonance** Finally, a few of these concerns are discussed from a basic physics understanding point of view. If one takes a monochromatic and absolutely coherent light wave that enters a high-finesse optical resonator (i.e. a Gaussian beam, perfectly mode-matched to only excite Gaussian modes for simplicity) three things can basically happen: first, if a multitude of the

---

<sup>5</sup>The build-up time for a cavity with losses would even be longer (e.g. due to absorption or scattering)

<sup>6</sup>The scanning could be performed by tuning the cavity length with a piezoelectric transducer (PZT)

half wavelength of the wave fits exactly into the resonator one will have resonant conditions due to the absence of any phase shift between the multiple reflections, i.e. after several round-trips all of the amplitudes interfere constructively, and the intensity (the square of the amplitudes) increases to an absolute maximum, i.e. a steady state emerges. Second, if the frequency does not match exactly the resonator frequency but is within the linewidth of the cavity mode, a certain phase shift is introduced that increases with each reflection at the mirrors. After several round-trips this phase shift can reach  $\pi$  and the wave interferes destructively. Therefore, for a wave that does not exactly match the resonance frequency of an optical resonator, the build-up of intra-cavity resonance will settle at a lower steady state, leading to a lower cavity output intensity. Third, if the frequency of an incident wave is far away from being within a cavity mode linewidth, and is consequently located somewhere else in the free spectral range, the deviation of phase between a wave in each reflection is large, and the intra-cavity intensity build-up is almost zero. Nevertheless, the photons of this wave propagate according to their life-time (ring-down time) within the resonator back and forth but interfere with some sort of a chaotic phase relationship.

One should note, that in each reflection there will be some leakage of the waves out of the resonator, according to the transmission coefficient of the mirrors (and probably absorption if one takes into account). This leads to some measurable signal intensity on either sides of the resonator - in transmission and in reflection. While the transmitted signal is high on resonance, as discussed above, one investigates now the case of a non-resonant cavity, assuming that the frequency of the input beam is far off a cavity mode. Then the output signal intensity will be very small due to the high reflectivity of the mirrors and the involved low transmission features. For instance, if one neglects losses, then one can assume that for a reflectivity of 0.9998 the transmission coefficient is at most 0.0002. If the wave enters the cavity, first the intensity is transmitted by a factor of 0.0002 and again by the same factor when it passes the second mirror. It might be a bit hilarious to mention but this means a transmission of the field intensity with a coefficient of  $4 \times 10^{-8}$ . And due to losses this amount decreases with each round trip even further. To summarize this: if the frequency of a wave is far off resonance, the amount of intensity that is transmitted through a high finesse cavity is extremely small and hard to detect. And due to the fact that the ratio of the free spectral range to the cavity mode linewidth is given by the finesse, it is not hard to imagine that for a free running laser in combination

with a high finesse cavity ( $\mathcal{F} \gtrsim 10^4$ ), it is far more likely to be off than on resonance and therefore the cavity transmission signal is almost zero.

If one now takes a broadband light source that is still absolutely coherent (with the awareness that this does not exist), one can think of it as a combination of the three cases presented above. Since the wave equation that is based on Maxwell's equations is linear, all of the waves within the resonator can be superimposed and exist for themselves independently within the resonator. According to the overlap of the linewidths of the laser source and the cavity mode, there will be some transmission in the open spectral window of the cavity mode. Nevertheless, the intensity of this transmitted wave is limited to the intensity of the input wave. This is a consequence of the Airy-formula. The transmitted intensity for a lossless mirror cavity is equal to the input intensity. But the narrow cavity transmission linewidth cuts out only a very narrow part of this broadband source, leading to a much smaller intensity at the output than at the input. One can think of it as a source with a broad spectral distribution of optical power that is filtered by a narrow frequency band-pass. So far only absolutely coherent light was considered. If one takes now a light wave with a broad spectrum that is not absolutely coherent but has a coherence time in the order of, or greater than, the time-constant of the resonator, then one basically has the same discussion as above. But if the coherence time is smaller than the time constant, one will see destructive interference again, even if the frequency of a wave matches the resonance frequency. This is because of the fluctuating phase of the incident wave, which leads to a loss of a defined phase relationship between the multiple reflections, preventing constructive interference. This leads to a lower steady state intra-cavity field, and consequently to a lower output intensity of the cavity. What one could do is to let enter the wave into the cavity only for a duration of time that matches its coherence time, and to investigate the output intensity. The build-up of intra-cavity intensity would now be the same as in the case of the broad-banded and absolutely coherent light source, except for the fact that the intensity build-up is stopped if the wave gets incoherent, and one ends up with a lower intra-cavity field as for a coherent wave. So far the incoherence of the source has been discussed. But what if the resonance frequency of the cavity was not stable? Consider again a monochromatic absolutely coherent wave that is incident on the cavity, and assume its frequency is equivalent to the initial resonance frequency of the cavity. If the light wave traveling between the two mirrors is very fast in comparison to the movement of the vibrating mirrors, after some round trips the length of the cavity has changed

due to these vibrations, and therefore the wave experiences essentially a phase shift at this point. After another sequence of round trips this happens again and so forth. One sees that this uncertainty of resonator length introduces a certain amount of phase noise along with at least partial destructive interference again. However, if the period length of these vibrations is longer than the build-up time of the resonator, it would have no significant influence on intensity build-up to reach a steady resonant state. Consequently, this means one has to comply with both: first choose an injection time that is lower than the coherence time of the laser source, and second, to choose a injection time that is lower than the period of mechanical vibrations, and going for the shorter time span of those two.

### **3.1 Summary and Conclusion**

In the beginning the author was entrusted with the demanding aim of frequency stabilizing a QCL for the use in spectroscopic applications at a chemical institute, where people had no theoretic nor practical experience with resonant optical cavities. Since at this time even the author, a physicist, had no special experience within this field, a study of the respective literature was carried out. Some components were chosen and purchased for the setup to complete the existing equipment. A first approach was accomplished on the bench but showed no results. Based on some measurements it soon became clear that electronic noise could have adverse influence on the build-up of resonant conditions. An iterative process of noise investigation and improvement started. Several components were identified of emitting electronic noise or being receptive for it and were consequently eliminated or replaced. Some of the components originated from a previous setup and contributed fairly strong to the system's noise-spectrum. Again the respective literature was consulted to attain a maximum improvement of the system's noise. A spectrum analyzer was brought into service for this purpose, and different actions in grounding, shielding, as well as signal-filtering were set. At this point there was still no evidence that would have accounted for the emergence of resonant conditions within the resonator. Once again some intensive research of the respective literature on lasers and QCLs in particular followed, and led to the - up to this time overseen - insight that the linewidth of a laser is directly linked to its coherence time. This research also uncovered the fact that the natural linewidth of a free running QCL could be significantly larger than the mode-linewidth of the used high-finesse optical resonator, which



suggested that the build-up of resonance was very unlikely. The passive stability of the resonator was identified as being of crucial importance for the achievement of resonant conditions and for implementing the PDH-technique. Therefore a housing was built up to shield the experimental setup against air-flows and acoustic noise. Finally, these actions were rewarded: weak signals indicated a partial build-up of intra-cavity intensity and motivated the emergence of short lasting cavity-resonances occurring from time to time. After overcoming all kinds of technical difficulties in a challenging chain of consistently appearing problems, this successful proof of principle may be classified as a remarkable result. However, further improvements have to be carried out to establish a stable reference cavity and to reach the laser frequency stabilization with the narrow linewidth features that were initially intended. The benefits of a consequential large intensity increase could serve for future spectroscopic applications. With no doubt the results of this work provides a solid basis to work with and paves the way for further developments.

## **3.2 Outlook**

The most important adaptations that have to be carried out to successfully implement the PDH-technique are more or less of the following: the passive resonator stability has to be increased against vibrations even further by use of a stable mirror cell. The LF magnetic shielding has to be improved by use of shielded twisted pair cables and maybe mu-metal housings. The utilization of a laser driver with even lower current noise density should be concerned. As an interesting experiment the natural linewidth of the employed QCL could be determined to assess the actual mismatch of the laser linewidth with respect to the cavity mode-linewidth.

# Bibliography

- [1] **J. Faist, F. Capasso, D.L. Sivco, A.L. Hutchinson, A.Y. Cho**, *Quantum Cascade Laser*. Science 264. p.553, **1994** [10](#), [13](#)
- [2] **R. F. Curl et al.**, *Quantum cascade lasers in chemical physics*. Chemical Physics Letters 487. 1-18, **2010** [9](#), [10](#), [11](#)
- [3] **F.K. Tittel, Y. Bakhirkin, R.F. Curl, A. Kosterev , R. Lewicki, S. So, G. Wysocki**, *Quantum Cascade Laser based Trace Gas sensor Technology: Recent Advances and Applications*. IEEE SENSORS Conference, 1-4244-1262-5/07, **2007** [9](#), [11](#)
- [4] **B. Paldus, A. Kachanov**, *An historical overview of cavity-enhanced methods*. Canadian Journal of Physics 83: 975-999, **2005** [9](#)
- [5] **J. Faist, C. Gmachl, F. Capasso, C. Sirtori, D.L. Sivco, J.N. Baillargeon, A.Y. Cho**, *Distributed feedback quantum cascade lasers*. Applied Physics Letters 70, p. 2670, **1997** [12](#)
- [6] **A. Hugi, R. Maulini, J. Faist**, *External cavity quantum cascade laser*. Semicond. Sci. Technol. 25, 083001, **2010** [12](#)
- [7] **M. S. Vitiello, G. Scalari, B. Williams, P. De Natale**, *Quantum cascade lasers: 20 years of challenges*. Optics Express Vol. 23, No. 4, p. 5167, **2015** [12](#), [13](#)
- [8] **A.L. Schawlow, C.H. Townes** , *Infrared and Optical Masers*. Physical Review, Vol. 112, No. 6, p. 1940, **1958** [12](#)
- [9] **C.H. Henry**, *Theory of the Linewidth of Semiconductor Lasers*. IEEE Journal of Quantum Electronics, Vol. QE-18, No. 2, p. 259, **1982** [12](#), [13](#)

- [10] **M. Yamanishi et al.**, *Theory of the Intrinsic Linewidth of Quantum-Cascade Lasers: Hidden Reason for the Narrow Linewidth and Line-Broadening by Thermal Photons*. IEEE Journal of Quantum Electronics, Vol. 44, No. 1, p. 12, **2008** [13](#)
- [11] **S. Bartalini et al.**, *Observing the intrinsic linewidth of a quantum-cascade laser: beyond the Schawlow-Townes limit*. arXiv:0912.2683v2 [physics.optics], **2010** [13](#), [72](#)
- [12] **L. Tombez et al.**, *Frequency noise of free-running 4.6  $\mu\text{m}$  distributed feedback quantum cascade lasers near room temperature*. Optics Letters 36, issue 16, 3109-3111, **2011** [13](#), [40](#)
- [13] **L. Tombez et al.**, *Linewidth of a quantum-cascade laser assessed from its frequency noise spectrum and impact of the current driver*. Appl Phys B. 109:407-414, **2012** [13](#)
- [14] **B.E.A. Saleh, M.C. Teich**, *Fundamentals of Photonics*. Wiley Series in Pure and Applied Optics, 2nd Ed., **2007** [15](#), [16](#), [17](#), [21](#), [23](#), [24](#), [26](#)
- [15] **H. Kogelnik, T. Li**, *Laser Beams and Resonators*. Proceedings of the IEEE Vol. 54, No. 10, p. 1312-1329, **1966**
- [16] **W. Demtröder**, *Experimentalphysik 2: Elektrizität und Optik*. Springer Verlag. 6. Auflage, **2013** [20](#), [24](#), [57](#)
- [17] **G. Berden, R. Engeln**, *Cavity Ring-Down Spectroscopy - Techniques and Applications*. Wiley. Blackwell Publishing Ltd. **2009** [25](#), [26](#), [51](#), [70](#)
- [18] **G.A. Reider**, *Photonik - Eine Einführung in die Grundlagen*. Springer Verlag, 3. Auflage, **2012** [25](#), [72](#), [76](#)
- [19] **Eric. D. Black**, *An introduction to Pound-Drever-Hall laser frequency stabilization*. Am. J. Phys. Vol. 69, No. 1, **2001** [29](#), [30](#), [31](#), [33](#), [34](#), [35](#)
- [20] **R.W.P. Drever et al.**, *Laser phase and frequency stabilization using an optical resonator*. Appl. Phys. B: Photophys. Laser Chem. 31, 97-105, **1983** [28](#), [30](#), [35](#), [72](#)

- [21] **C.E. Liekhus-Schmaltz et al.**, *Understanding Pound-Drever-Hall locking using voltage controlled radio-frequency oscillators: An undergraduate experiment*. arXiv:1108.0960v2 [physics.ed-ph], **2011** [29](#)
- [22] **D. Anderson**, *Alignment of resonant optical cavities*. Applied Optics, Vol. 23, No. 17, p. 2944, **1984** [26](#)
- [23] **Henry W. Ott**, *Electromagnetic Compatibility Engineering*. Wiley, **2009** [53](#), [54](#), [55](#), [56](#), [57](#), [58](#), [59](#), [60](#), [61](#), [62](#)
- [24] **H. Wolfspurger**, *Elektromagnetische Schirmung - Theorie und Praxisbeispiele*. Springer Verlag, **2008** [57](#), [59](#)
- [25] **G. Di Domenico, S. Schilt, P. Thomann**, *Simple approach to the relation between laser frequency noise and laser line shape*. Applied Optics, issue 25, 4801-4807, **2010** [68](#)
- [26] **J. Morville, D. Romanini et al.**, *Effects of laser phase noise on the injection of a high-finesse cavity*. Optical Society of America, Applied Optics Vol. 41, No. 33, **2002** [69](#), [71](#), [72](#)
- [27] **K. Nakagawa et al.**, *Highly sensitive detection of molecular absorption using a high finesse optical cavity*. Elsevier, Optics Communications 107, p. 369-372, **1994** [72](#)
- [28] **E. Fasci et al.**, *Narrow-linewidth quantum cascade laser at 8.6 um*. Optics Letters, Vol. 39, No. 16, p. 4946, **2014** [74](#)
- [29] **L. Tombez et al.**, *Active linewidth-narrowing of a mid-infrared quantum cascade laser without optical reference*. Optics Letters, Vol. 38, No. 23, p. 5079, **2013** [75](#)
- [30] **L. Tombez et al.**, *Physical Origin of Frequency Noise and Linewidth in Mid-IR DFB Quantum Cascade Lasers*. Conference Paper, DOI: 10.1364/CLEO\_SI.2013.CM1K.3, **2013** [75](#)
- [31] **CRD Optics Inc.**, <http://www.crd-optics.com/crd-mirrors-ir.html> [43](#)
- [32] **Electro-Optics Technology Inc.**, <http://www.eotech.com/content/userfiles/Mesos-4um%20Faraday%20Rotators%20and%20Isolators.pdf> [42](#)

- [33] **refractiveindex.info**,  
<http://refractiveindex.info/?shelf=main&book=ZnSe&page=Connolly> 43
- [34] **Toptica Photonics**, [http://www.toptica.com/fileadmin/user\\_upload/products/Diode\\_Lasers/Research\\_Grade/Control\\_Electronics/Digital\\_Feedback\\_Controlyzer/Digilock\\_Manual.pdf](http://www.toptica.com/fileadmin/user_upload/products/Diode_Lasers/Research_Grade/Control_Electronics/Digital_Feedback_Controlyzer/Digilock_Manual.pdf) 43
- [35] **J.L. Elkhorne**, *Edison - The Fabulous Drone*. 73 Magazine, Vol XLVI, No. 3, p. 52, March **1967** 4
- [36] **Wolfram Demonstrations Project**,  
<http://demonstrations.wolfram.com/GaussianBeamPropagationThroughTwoLenses> 85

# Chapter 4

## Appendix

### Code of Mode-Matching Calculation

The content of the following pages provides the Wolfram Mathematica code that was worked out to calculate the mode-matching parameters. The plots of the beam-envelope are based on some code of a Wolfram Demonstration [36] that was modified. These plots only show the propagation of the incident beam (orange) to the mode-matching lens (thin, black vertical line segment) where the beam gets transformed (blue). In addition, the cavity mirrors are shown (red). The beam waist of the transformed (blue) beam is indicated by a vertical black line-segment. If the mirror's index of refraction  $n_2$  is modeled to be equal to that of air, and the mirror thickness  $s$  is modeled to be zero, then the obtained beam-waist is located exactly in the center of the cavity. This can be explained by the lens-effect of the entrance mirror, which shifts the beam waist of the transformed (blue) beam into the center of the cavity (not shown in the plots).

Finally, some [photographs](#) are shown that were taken during the course of this work.

```

In[372]:= (* Cavity mode-matching calculation for one lens *)
(* ***** *)
(* ray transfer matrices *)
M1 =  $\begin{pmatrix} 1 & d1/n1 \\ 0 & 1 \end{pmatrix}$ ; (* free space propagation by d1 from laser waist to lens in air n1*)
M2 =  $\begin{pmatrix} 1 & 0 \\ -1/f & 1 \end{pmatrix}$ ; (* lens *)
M3 =  $\begin{pmatrix} 1 & d2/n1 \\ 0 & 1 \end{pmatrix}$ ;
(* free space propagation by d2 from lens to cavity mirror in air n1 *)
M4 =  $\begin{pmatrix} 1 & \frac{s}{n2} \\ \frac{-n1+n2}{R} & 1 + \frac{s(-n1+n2)}{n2 R} \end{pmatrix}$ ; (* concave cavity mirror with radius R,
thickness s, refractive index n2 *)
M5 =  $\begin{pmatrix} 1 & L/(2 n1) \\ 0 & 1 \end{pmatrix}$ ;
(* free space propagation to the center of cavity to the waist in air n1 *)
MT = Dot[M5, M4, M3, M2, M1]; (* ABCD - matrix product - mind the order of the matrices *)
AA = MT[[1, 1]]; (* select matrix elements and assign to A,B,C,D *)
BB = MT[[1, 2]];
CC = MT[[2, 1]];
DD = MT[[2, 2]];

(* parameters - all lengths in meters *)
λ = 4.59×10-6; (* laser wavelength *)
n1 = 1.00028; (* refractive index of air n1 = 1.00028 *)
n2 = 2.432; (* refractive index of ZnSe-mirror n2 = 2.432,
source: refractiveindex.info *)
s = 0.00635; (* mirror thickness *)
R = 6.0; (* cavity mirror radius *)
L = 1.00; (* cavity length / m *)
f = 0.50; (* focal length of mode matching lens *)
c = 299792458.0; (* speed of light in vacuum m/s *)
wi = 0.000795/2.0; (* waist radius of incident beam *)
qi = i π wi2/λ; (* complex beam parameter at waist of incident beam *)
q0 = i π w02/λ; (* complex beam parameter at cavity waist *)
g1 = 1 - L/R; (* g1 parameter of cavity *)
g2 = 1 - L/R; (* g2 parameter of cavity *)
w0 = (L λ / π)(1/2) (g1 g2 (1 - g1 g2) / (g1 + g2 - 2 g1 g2)2)(1/4);
(* intra-cavity beam waist radius *)

sol = Solve[{AA - DD (w0/wi)2 == 0, CC (π w0 wi / λ)2 + BB == 0}, {d1, d2}];
(* numeric solve of beam propagation equation *)
(* solution d2 is the distance of lens from the cavity input mirror *)
d1sol = sol[[All, 1, 2]]; (* assign elements of equation solve for d1 *)
d2sol = sol[[All, 2, 2]]; (* assign elements of equation solve for d2 *)

Print["* * Results of calculation * * "]
Print["for a lens with focal length f: ", 1000 f, "mm, cavity length L: ", 1000 L "mm"]
Print["and incident waist radius wi: ", 106 wi "μm"]
Print["the cavity waist radius w0 is: ", 106 w0 "μm"]
Print["* * * * * "]

```

```

Print["The distances are: "]
Print["Solution 1 for d1: ", 1000 d1sol[[1]], " mm"]
Print["Solution 1 for d2: ", 1000 d2sol[[1]], " mm"]
Print["Beam waist after lens: ", 1000 z00b[wi, d1sol[[1]]] " mm"]
Print["* * * * * "]
Print["Solution 2 for d1: ", 1000 d1sol[[2]], " mm"]
Print["Solution 2 for d2: ", 1000 d2sol[[2]], " mm"]
Print["Beam waist after lens: ", 1000 z00b[wi, d1sol[[2]]] " mm"]
Print["* * * * * "]
Print["Mind: negative or complex values are
      not possible - change incident waist size and/or focal length"]

NextBeamWaist[W00_, z0_] := (* W00...incident waist,
z0...position of lens from incident waist *)
Module[{bw = W00},

  W1 = W00  $\sqrt{1 + \left(\frac{\lambda \times z0}{\pi (W00)^2}\right)^2}$  ; (*beam width at the first lens*)

  R0 = z0  $\left(1 + \left(\frac{\pi (W00)^2}{\lambda \times z0}\right)^2\right)$  ;

  (*radius of curvature at the first lens, before transformation*)

  R1 =  $\frac{R0 \times f}{f - R0}$  ; (*radius of curvature at the first lens, after transformation*)

  bw = W1  $\sqrt{\frac{1}{1 + \left(\frac{\pi (W1)^2}{\lambda \times R1}\right)^2}}$  ] (*the new beamwaist after transformation by the lens*)

NextBeamWaistPos[W00_, z0_] := (* W00...incident waist,
z0...position of lens from incident waist *)
Module[{wp = z0},

  W1 = W00  $\sqrt{1 + \left(\frac{\lambda \times z0}{\pi (W00)^2}\right)^2}$  ;

  R0 = z0  $\left(1 + \left(\frac{\pi (W00)^2}{\lambda \times z0}\right)^2\right)$  ;

  R1 =  $\frac{R0 \times f}{f - R0}$  ;

  wp =  $\frac{-R1}{1 + \left(\frac{\lambda \times R1}{\pi (W1)^2}\right)^2}$  ] (*the position where the first new beamwaist appears,
after transformation by the first lens*)

W01[W00_, z00a_] := NextBeamWaist[W00, z00a] (* beam waist after lens *)
z00b[W00_, z00a_] := NextBeamWaistPos[W00, z00a] (* beam waist position after lens *)
lens[z_] := Graphics[Circle[{z, 0}, {0.003, 0.001}]]

```



```

func1sol1 = wi  $\sqrt{1 + \left(\frac{\lambda \times z}{\pi (wi)^2}\right)^2}$ ; (* beam envelope from incident waist to lens *)

func2sol1 = W01[wi, d1sol[[1]]]  $\sqrt{1 + \left(\frac{\lambda \times (z - z00b[wi, d1sol[[1]]] - d1sol[[1]])}{\pi (W01[wi, d1sol[[1]])^2}\right)^2}$ ;

(* beam envelope from lens to cavity *)
Show[Plot[{func1sol1, -func1sol1, func2sol1, -func2sol1}, {z, -2.0, 2.0},
  PlotStyle -> {Orange, Orange, Blue, Blue}, PlotLabel -> "Solution 1 (not possible)",
  AxesLabel -> {Style["distance d / m", Italic], Style["beam waist w / m", Italic]}],
lens[d1sol[[1]]], Graphics[{Thick,
  Line[{d1sol[[1]] + z00b[wi, d1sol[[1]]], -W01[wi, d1sol[[1]]],
    {d1sol[[1]] + z00b[wi, d1sol[[1]]], W01[wi, d1sol[[1]]]}]},
Graphics[{Thick, Red, Line[{d1sol[[1]] + d2sol[[1]], -0.001},
  {d1sol[[1]] + d2sol[[1]], 0.001}]}],
Graphics[{Thick, Red, Line[{d1sol[[1]] + d2sol[[1]] + L, -0.001},
  {d1sol[[1]] + d2sol[[1]] + L, 0.001}]}]}
]]

func1sol2 = wi  $\sqrt{1 + \left(\frac{\lambda \times z}{\pi (wi)^2}\right)^2}$ ;

func2sol2 = W01[wi, d1sol[[2]]]  $\sqrt{1 + \left(\frac{\lambda \times (z - z00b[wi, d1sol[[2]]] - d1sol[[2]])}{\pi (W01[wi, d1sol[[2]])^2}\right)^2}$ ;

Show[Plot[{func1sol2, -func1sol2, func2sol2, -func2sol2},
  {z, -0.2, 3.0}, PlotRange -> {{-0.2, 3.0}, {-0.01, 0.01}},
  PlotStyle -> {Orange, Orange, Blue, Blue}, PlotLabel -> "Solution 2",
  AxesLabel -> {Style["distance d / m", Italic], Style["beam waist w / m", Italic]}],
lens[d1sol[[2]]], Graphics[{Thick,
  Line[{d1sol[[2]] + z00b[wi, d1sol[[2]]], -W01[wi, d1sol[[2]]],
    {d1sol[[2]] + z00b[wi, d1sol[[2]]], W01[wi, d1sol[[2]]]}]},
Graphics[{Thick, Red, Line[{d1sol[[2]] + d2sol[[2]], -0.001},
  {d1sol[[2]] + d2sol[[2]], 0.001}]}],
Graphics[{Thick, Red, Line[{d1sol[[2]] + d2sol[[2]] + L, -0.001},
  {d1sol[[2]] + d2sol[[2]] + L, 0.001}]}]}
]]

```

Solve::ratnz : Solve was unable to solve the system with inexact coefficients.

The answer was obtained by solving a corresponding exact system and numericizing the result. >>

```

* * Results of calculation * *

for a lens with focal length f: 500.mm, cavity length L: 1000.mm
and incident waist radius wi: 397.5  $\mu$ m
the cavity waist radius w0 is: 1556.56  $\mu$ m

* * * * *

The distances are:

Solution 1 for d1: 393.893 mm
Solution 1 for d2: -1521.27 mm
Beam waist after lens: -655.633 mm

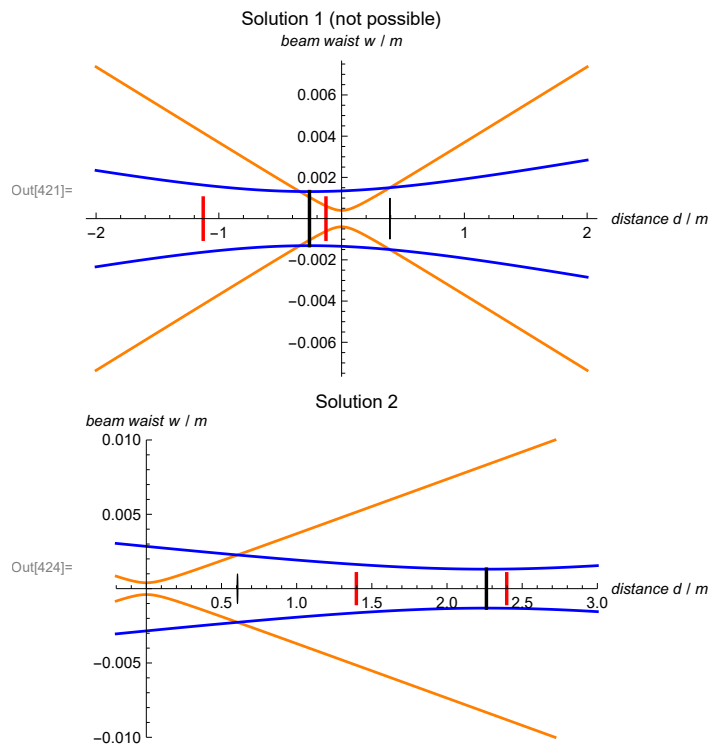
* * * * *

Solution 2 for d1: 606.387 mm
Solution 2 for d2: 790.687 mm
Beam waist after lens: 1655.69 mm

* * * * *

Mind: negative or complex values are not
      possible - change incident waist size and/or focal length

```



```

In[1]:= (** Explicit form of the ABCD ray-transfer matrix **)

M1 =  $\begin{pmatrix} 1 & d1/n1 \\ 0 & 1 \end{pmatrix}$ ;

(* free space propagation by d1 from laser waist to lens in air n1*)

M2 =  $\begin{pmatrix} 1 & 0 \\ -1/f & 1 \end{pmatrix}$ ; (* lens *)

M3 =  $\begin{pmatrix} 1 & d2/n1 \\ 0 & 1 \end{pmatrix}$ ;

(* free space propagation by d2 from lens to cavity mirror in air n1 *)

M4 =  $\begin{pmatrix} 1 & \frac{s}{n2} \\ \frac{-n1+n2}{R} & 1 + \frac{s(-n1+n2)}{n2 R} \end{pmatrix}$ ; (* concave cavity mirror with radius R,
thickness s, refractive index n2 *)

M5 =  $\begin{pmatrix} 1 & L/(2 n1) \\ 0 & 1 \end{pmatrix}$ ;

(* free space propagation to the center of cavity to the waist in air n1 *)

MT = Dot[M5, M4, M3, M2, M1] // MatrixForm

```

Out[1]//MatrixForm=

$$\begin{pmatrix} 1 + \frac{L(-n1+n2)}{2 n1 R} - \frac{d2 \left( 1 + \frac{L(-n1+n2)}{2 n1 R} \right) \frac{s}{n2} + \frac{L \left( 1 + \frac{(-n1+n2)s}{n2 R} \right)}{2 n1}}{f} & d1 \left( 1 + \frac{L(-n1+n2)}{2 n1 R} - \frac{d2 \left( 1 + \frac{L(-n1+n2)}{2 n1 R} \right) \frac{s}{n2} + \frac{L \left( 1 + \frac{(-n1+n2)s}{n2 R} \right)}{2 n1}}{f} \right) \\ \frac{-n1+n2}{R} - \frac{1 + \frac{d2(-n1+n2)}{n1 R} + \frac{(-n1+n2)s}{n2 R}}{f} & 1 + \frac{d2(-n1+n2)}{n1 R} + \frac{(-n1+n2)s}{n2 R} + \frac{d1 \left( \frac{-n1+n2}{R} - \frac{1 + \frac{d2(-n1+n2)}{n1 R} + \frac{(-n1+n2)s}{n2 R}}{f} \right)}{n1} \end{pmatrix}$$

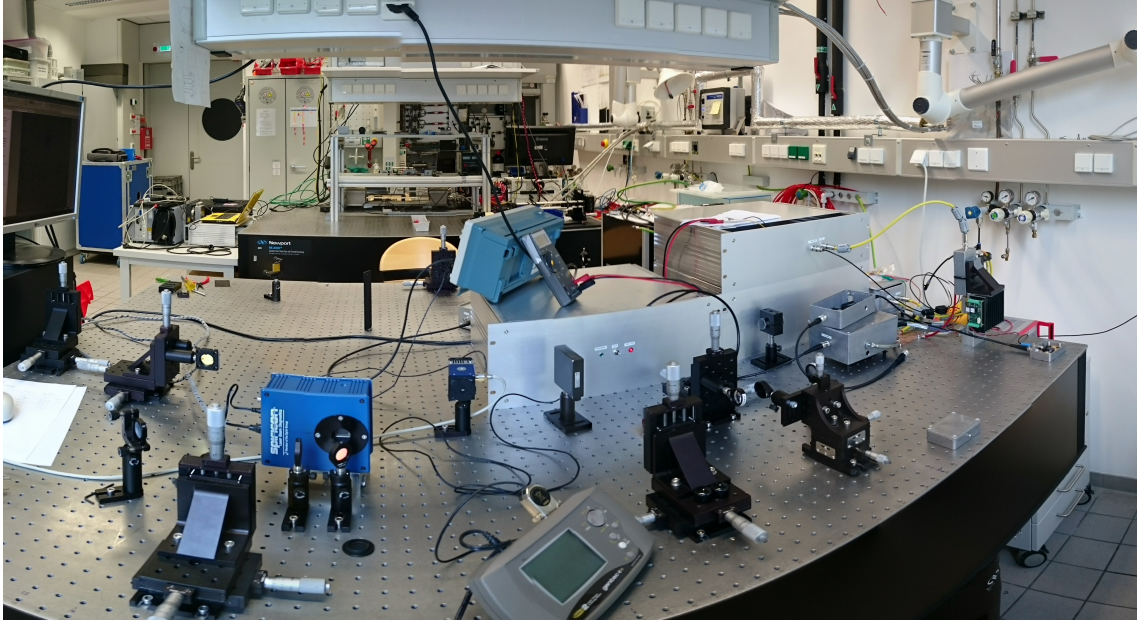


Figure 4.1: Some parts of the setup before it was covered with a housing. To the very right end of the table, the QCL source with the protection circuit attached can be seen.

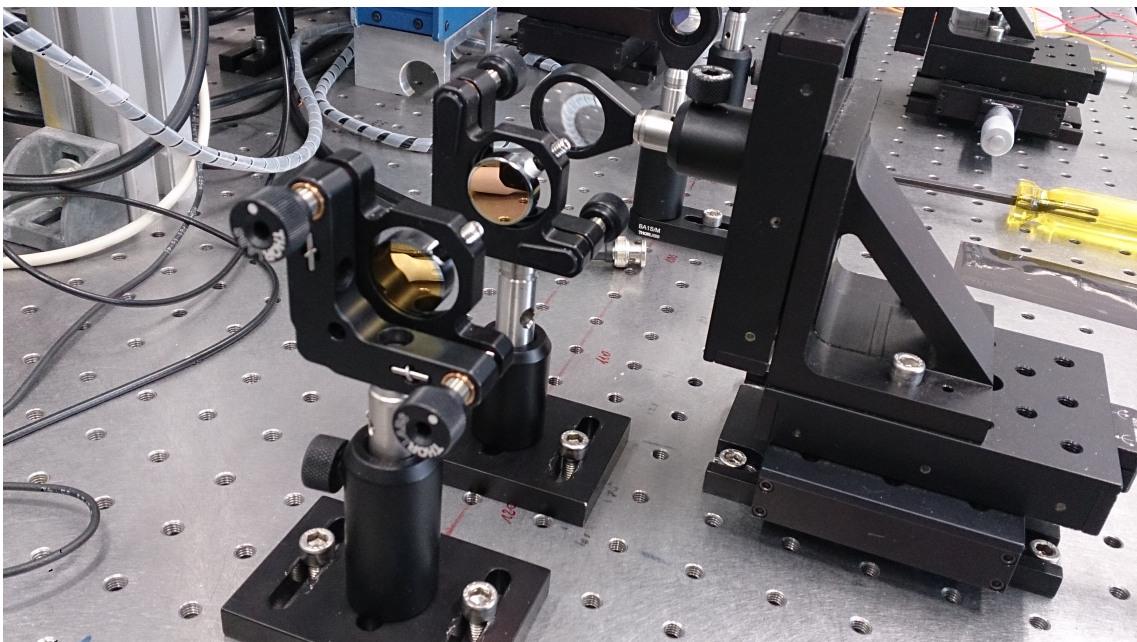


Figure 4.2: High reflective mirrors in a very early stage of the experimental setup (these mirror mounts were replaced later)